Plate interface rheological switches during subduction infancy: control on slab penetration and metamorphic sole formation

P. Agard[1,2,*], P. Yamato[3], M. Soret[1], C. Prigent[4], S. Guillot[4],

A. Plunder[1], B. Dubacq[1], A. Chauvet[5], P. Monié[5]

[1]Sorbonne Universités, UPMC Univ Paris 06, CNRS, Institut des Sciences de la Terre de Paris (iSTeP), 4 place Jussieu 75005 Paris, France

[2]Institut Universitaire de France, F-75005 Paris, France

[3]Géosciences Rennes, Université de Rennes 1, CNRS UMR 6118, F-35042 Rennes Cedex, France

[4]Univ. Grenoble Alpes, CNRS, ISTerre, F-38000 Grenoble, France

[5]Géosciences Montpellier, Univ Montpellier 2, CNRS, F-34095 Montpellier, France

*corresponding author: philippe.agard@upmc.fr

Abstract

Subduction infancy corresponds to the first few million years following subduction initiation, when slabs start their descent into the mantle. It coincides with the transient (yet systematic) transfer of material from the top of the slab to the upper plate, as witnessed by metamorphic soles welded beneath obducted ophiolites. Combining structure-lithology-pressure-temperature-time data from metamorphic soles with flow laws derived from experimental rock mechanics, this study highlights two main successive rheological switches across the subduction interface (mantle wedge vs. basalts, then mantle wedge vs. sediments; at ~800°C and ~600°C, respectively), during which interplate mechanical coupling is maximized by the existence of transiently similar rheologies across the plate contact. We propose that these rheological switches hinder slab penetration and are responsible for slicing the top of the slab and welding crustal pieces (high- then low-temperature metamorphic soles) to the base of the mantle wedge during subduction infancy. This mechanism has implications for the rheological properties of the crust and mantle (and for transient episodes of accretion/exhumation of HP-LT rocks in mature subduction systems) and highlights the role of fluids in enabling subduction to overcome the early resistance to slab penetration.

Keywords:

Subduction, metamorphic sole, rheology, plate interface, slab dehydration, mechanical coupling

1. Introduction

Understanding subduction initiation, in both space and time, has been a challenge since the advent of plate tectonics (Dewey, 1976; Regenauer-Lieb et al., 2001; Gurnis et al., 2004). What is referred to as "subduction initiation" in the literature encompasses two different concepts and periods: (i) how and where subduction nucleates (i.e., what triggers the beginning of subduction; e.g., Regenauer-Lieb et al., 2001; Stern, 2004), and (ii) how subduction proceeds over the first few million years of its history ("subduction infancy"; Stern and Bloomer, 1992).

This study focuses on subduction infancy, when a newly born slab starts its descent into the mantle and when the thermal regime of the subduction zone progressively cools down before reaching steady-state (e.g., Syracuse et al., 2010; Plunder et al., 2015; Figs. 1a,b). The only rock remnants of this elusive geodynamic step are thin (~10-500 m) metamorphosed slivers of oceanic crust (metamorphic soles; Williams and Smyth, 1973; Wakabayashi and Dilek, 2000) found beneath pristine, 100-1000 km long, ≤10-15 km thick fragments of oceanic lithosphere emplaced on top of continents as ophiolites (Coleman, 1981; Nicolas, 1989; Fig. 1c).

Metamorphic soles correspond to upper crustal material from the downgoing slab (with variable proportions of basalts and pelagic sediments; Spray et al. 1984; Boudier et al., 1988) and have long been recognized as formed during the first few My of intra-oceanic subduction (Fig. 1b; Dewey, 1976; Spray et al., 1984; Dewey and Casey, 2013). Their formation would result from heat transfer from the upper plate mantle and/or shear heating when the slab enters the mantle and heats up (Dewey, 1976; Hacker, 1990). Explaining how such thin metamorphosed tectonic slivers of oceanic crust get welded ("underplated") to the upper plate along hundreds of km (e.g., Oman, Turkey: Hacker and Gnos, 1997; Çelik et al., 2011) is essential for understanding mechanical coupling

during subduction infancy (and possibly during later subduction), but has so far remained enigmatic (Jamieson, 1981; Dewey and Casey, 2013).

This problem is herein addressed by (i) compiling worldwide characteristics of metamorphic soles (i.e., lithologies, internal organization, thicknesses, thermobarometric constraints), augmented by refined estimates for their pressure-temperature (P-T) conditions of formation using thermodynamic modelling and by (ii) calculating effective viscosities of materials present along the plate interface from known rheological properties for the crust and mantle (i.e., peridotite, basalt, sediment, serpentinite).

This study reveals the existence of rheological switches across the subduction interface, and proposes that these changes in rheological properties control slab penetration into the mantle and the formation of metamorphic soles during subduction infancy. This mechanism has implications for effective rheologies of the crust and mantle and for the general understanding of accretion processes and early slab dynamics.

2. Metamorphic soles: the record of subduction infancy

2.1 Metamorphic sole constitution

The main characteristics (i.e., structural position, lithologies, constitution) and P-T conditions of metamorphic soles worldwide are reviewed in figure 2 and Table 1. This synthesis shows that metamorphic soles are ubiquitous beneath non-metamorphosed ophiolites (e.g., Oman, Turkey, Papua, Newfoundland) and share similar characteristics regardless of the ophiolite or the detailed geological/geodynamical setting (Spray, 1984; Wakabayashi and Dilek, 2003). Radiometric ages of metamorphic soles and ophiolites generally fall within 1-2 My (e.g., Fig. 1d for Oman; Hacker et al., 1996; Rioux et al., 2013), suggesting the existence of a still warm (i.e., > 1000°C) upper plate mantle near the subduction interface.

Metamorphic soles comprise ~10 to ~500 m thick (Figs. 2b-c) highly strained and metamorphosed crustal rocks where amphibolitized metabasalt dominates, together with increasing

proportions of pelagic metasediment structurally downwards (mainly metaradiolarite, with intercalations of metatuff and metapelite downwards). Vertically, metamorphic soles exhibit an inverted metamorphic sequence with isograds subparallel to the basal peridotite foliation (Spray, 1984). They grade steeply from thin high temperature (HT) granulite/amphibolite facies lithologies adjacent to the overlying peridotites (> 700-850°C; Fig. 2d; e.g., McCaig, 1983; Jamieson, 1986) to thicker amphibolite/greenschist facies low temperature soles (LT; ~550-650°C; Table 1). This temperature trend is not continuous, however, since the structurally and thermally lower LT sole is arguably formed later, and at lower pressure than the HT sole, by successive stacking of increasing amounts of metasediment (e.g., Malpas, 1979; Casey and Dewey, 1984; Jamieson, 1986; Fig. 2d). Whenever radiometric constraints are available, HT soles are coeval or slightly older than LT soles, yet within ~2 My (e.g., for Oman: Fig. 1d; Hacker et al., 1996; Roberts et al., 2016). HT soles and/or LT soles may be missing in places but wherever both are observed, and not disturbed by obvious later tectonics, HT soles are overlying LT soles.

High deformation in the HT and LT soles is marked by mylonites and complex recumbent folding. This deformation, however, is commonly less conspicuous in HT sole mafic amphibolites than in the LT soles (Jamieson, 1981; this study), due to the extent of recrystallization (e.g., Oman) and/or to the lack of lithological heterogeneities. Wherever (rarely) preserved, stretching lineations in the HT soles and LT soles strike differently (e.g., Newfoundland; Dewey and Casey, 2013), suggesting that boundary conditions and/or accretion dynamics may have been modified during sequential underplating.

Some earlier workers, on the basis of rare gabbroic occurrences (associated with dunite and locally intercalated between the mantle and the HT metamorphic amphibolite; Jamieson, 1981), suggested that the whole metamorphic sole could represent a metamorphosed, overturned limb of ophiolite crust (with sediments, basalts and gabbros from bottom to top; see also Wakabayashi and Dilek, 2003). This interpretation is however unlikely: (i) in contrast with the ophiolite crust, gabbros are extremely rare in the soles (and may represent small-scale intrusions in the mantle), (ii) HT mafic amphibolites tend to have a distinctive nature/geochemical signature (i.e., MORB

128 transitional to OIB or E-MORB; Dewey and Casey, 2013) and (iii) the overturned limb hypothesis
129 fails to explain why pressure conditions in the metasedimentary LT sole are lower than in the HT
130 sole located above (Gnos, 1998; section 2.2).

131 The mantle rocks immediately above the metamorphic sole are also highly deformed (Fig. 2d),
132 showing m- to hm-scale deformation patterns consistent with those observed in the underlying HT
133 sole (Boudier et al., 1988), pressure estimates equivalent to those of HT sole peak metamorphism
134 (Jamieson, 1981; McCaig, 1983) and porphyroclastic to ultramylonitic textures formed in the
135 temperature range of 1100°C down to ~700°C (Boudier et al., 1988; Michibayashi and Mainprice,
136 2004; Linckens et al., 2011b). This suggests that the base of the ophiolite mantle deformed and
137 cooled during subduction infancy and that, from a mechanical point of view, the metamorphic sole
138 should be considered as a threefold stack with, from bottom to top, the LT sole, the HT sole and the
139 base of the ophiolitic mantle sequence (hereafter noted as: LTsole\HTsole\basal peridotites).
140

141 ***2.2 P-T conditions of metamorphic soles***

142 Published P-T estimates for metamorphic sole formation (Fig. 3a; Table 1) spread along a high
143 to medium T/P gradient, which partly arises from the diversity and variable precision of
144 thermobarometric methods used. New P-T estimates for HT soles are provided here using
145 thermodynamic modelling. P-T phase diagrams for fixed bulk rock composition (pseudosections)
146 were calculated to constrain the conditions of HT sole formation using the Gibbs-free-energy
147 minimization software THERIAK/DOMINO (de Capitani and Petrakakis, 2010; with the updated
148 database of Holland and Powell (1998); tcdb55cc2d.bs) with the following solution models: Diener
149 et al. (2007) for amphibole, Green et al. (2007) for clinopyroxene, White et al. (2007) for
150 orthopyroxene, Holland et al. (1998) for chlorite, Baldwin et al. (2005) for plagioclase and Holland
151 and Powell (1998) for garnet. P-T conditions for LT soles are difficult to assess, unfortunately,
152 owing to the high variance of the assemblages and uncertainties in thermodynamic models.

153 A representative pseudosection (Fig. 3b) was calculated within the chemical system Na_2O–
154 CaO–FeO–MnO–MgO–Al_2O_3–SiO_2–H_2O for a typical mafic amphibolite (YE1302b; Lycian

ophiolite, W. Turkey) with garnet, clinopyroxene, plagioclase and amphibole. The corresponding sample comes from the region of Salda (South Western Turkey; N037°46'44" E029°56'21"), where garnet-clinopyroxene amphibolites are passing downwards, away from the contact with the overlying peridotite, to amphibolites and then to greenschist facies rocks. Spinel is replaced by plagioclase in the nearby peridotite, suggesting former equilibration of the rock at pressures > 0.8-1 GPa. At the thin section scale, garnet and clinopyroxene are intimately intergrown (with globular shape inclusions of clinopyroxene in garnet). Amphibole and plagioclase are found both in the matrix and as inclusions in garnet and clinopyroxene, and therefore formed during peak conditions. Clinopyroxene has diopside compositions with Mg# ~ 0.80 and a Ca content of 0.88 - 0.91 per formula unit (p.f.u.). The pyrope content in garnet ranges between 0.20-0.28 p.f.u. and plagioclase (when preserved) has an anorthite fraction of 0.2-0.3.

P-T conditions for the garnet–clinopyroxene–amphibole–plagioclase peak assemblage of sample YE1302b, using mineral isopleths, are 1.08 ± 0.1 GPa and 780 ± 40 °C. Water amounts were set to match amphibole modes (50-60 vol%). TiO_2 was neglected in the calculation as it enters mainly accessory minerals (rutile, titanite) and amphibole, in which titanium is not accounted for (Diener et al., 2007). The MnO content reproduces the observed garnet chemistry and ensures consistent garnet and clinopyroxene Fe-Mg exchange.

A similar range of estimates was obtained with phase diagrams for metamorphic soles from Turkey (in Kütahya; boxes in Fig. 3a; Table 1) and Oman (in Sumeini and Khubakhib; dashed boxes, Fig. 3a), pointing to definitely high P values for the upper HT soles when compared to the spread of published estimates (i.e., black dots in Fig. 3a). This conclusion is strengthened by the similarity of available mineral assemblages and compositions worldwide. These estimates are consistent with the presence of only subordinate amounts of melts in the HT soles (Gnos, 1998), suggesting that temperatures do not significantly exceed amphibolite dehydration melting (in agreement with predicted melt fractions < 5-10 vol% at 850°C, depending on pressure; Green et al., 2016).

2.3 Significance of metamorphic soles within thermal subduction regimes

The above compilation shows that conditions for metamorphic sole formation are remarkably similar worldwide and characterized by the accretion of HT soles that are thinner, more mafic, accreted earlier, at greater depths, at almost invariant P-T conditions (800 ± 50°C at 1.0 ± 0.2 GPa) and always on top of LT soles (equilibrated at ~600 ± 50°C at 0.5 ± 0.1 GPa).

These estimates are compared to peak conditions reached by oceanic rocks during later subduction, namely those for HT and LT eclogites (Fig. 3a; see Agard et al., 2009 for a review). Their contrasting P-T conditions exemplify the change in the subduction thermal gradient through time, from warm to cold, from peak burial conditions of ~800°C and 1.0 GPa to ~550°C and 2.5 GPa. Figure 3a shows that during subduction infancy and subsequent cooling, three rock types successively form from the upper crust of the down-going slab: (1) metamorphic soles within the first 1-2 My, along the hotter gradient, (2) HT oceanic eclogites postdating initiation by ~5 My, commonly exhumed in serpentinite mélanges with counter-clockwise P-T paths (arrows in Fig. 3a; e.g., Wakabayashi, 1990; Garcia-Casco et al., 2006), (3) LT oceanic eclogites formed after 5-10 My and, whenever exhumed, mostly as continuous tectonic slices.

Contrary to metamorphic soles, the fraction of eclogites exhumed worldwide is only rarely accreted to an upper plate ophiolite mantle. Figure 3a also shows that accretion largely overlaps the domain where serpentine is not stable.

Most HT metamorphic soles do not show later HP-LT metamorphism overprint, such as would be expected from progressive cooling if these rocks had remained at their depth of formation. The implication is that the HT soles formed at ~1 GPa must have been accreted and partly exhumed (together with the deformed base of the ophiolite mantle) during subduction infancy (i.e., before significant cooling of the subduction thermal regime), and later underplated below the undeformed ophiolite mantle.

3. Rheology of the plate interface and mechanical coupling during subduction infancy

A generic mechanical process is needed to explain how slices of crustal material from the slab get accreted to the mantle wedge (i) only during subduction infancy and (ii) in such a uniform manner. Accretion (or "underplating") of any tectonic slice across the subduction interface requires the combination of:

(i) an increase in mechanical coupling across the plate contact beyond some threshold, in order to preferentially localize strain and relative displacement elsewhere within the slab, along some other physical discontinuity (e.g., basalt vs. sediment, or basalt vs. sheeted dykes; Kimura and Ludden, 1995; Dewey and Casey, 2013),

(ii) some deformation mechanisms allowing for effective slicing within the slab. Whether slicing takes place through slow creep, fluid-mediated slip (such as slow slip events) or repeated regular earthquakes is unknown to date and beyond the scope of the present study.

Noteworthily, mechanical coupling is maximum when rheologies on both sides of the plate interface are similar: strain is otherwise localized and the interface is decoupled.

3.1 Effective viscosities of plate interface material constrained by rock mechanics

Flow laws derived from experimental rock mechanics (Table 2) are used to estimate the effective viscosity (η) of plate interface materials as a function of temperature (T). Figure 4a shows this dependency for rocks expected to lie at the base of the upper plate (peridotite, serpentinite) and at the top of the slab (basalt, sediment), using a strain rate ($\dot{\epsilon}$) derived from natural constraints (10^{-13} s^{-1} for Oman; Linckens et al., 2011b) and the following formula:

$$\eta = \frac{1}{2} A^{-\frac{1}{n}} \dot{\varepsilon}^{\frac{1-n}{n}} \exp\left(\frac{Q}{nRT}\right)$$

where n, A, Q and R correspond to the power-law exponent, the material constant, the activation energy and the gas constant, respectively.

The reader is referred to Karato (2010) and Hirth and Kohldstedt (2015) for reviews of flow laws of relevance for the mantle. These were derived from experiments on dry or wet olivine for

236 dislocation creep (e.g., Hirth and Kohlstedt, 2003) and for grain size dependent deformation
237 mechanisms such as diffusion creep (Hirth and Kholstedt, 2003; Faul and Jackson, 2007) and
238 dislocation-accommodated grain boundary sliding (disGBS; Hirth and Kohldstedt, 2003: Hansen et
239 al., 2011). Important independent constraints on mantle deformation along the plate interface come
240 from natural data on basal peridotites and mantle shear zones rooting in the deformed mantle base
241 of the ophiolite (Boudier et al., 1988; Linckens et al., 2011a,b). The evolution from 1100°C in
242 porphyroclastic peridotites to ~700°C in ultramylonites shows that (i) olivine grain size decreases
243 from ~2 mm to 10-50 μm and (ii) deformation mechanisms evolve at ~800-850°C from dislocation
244 creep to grain size sensitive creep, diffusion creep being the most likely dominant mechanism in
245 localized shear bands (the boundary between diffusion creep and disGBS is not well known
246 however; Linckens et al., 2011b).

247 Flow laws for metamorphic sole mafic rocks are scarce in comparison and can be approached
248 by using wet/dry diabase and mafic granulite. Flow laws are even scarcer for metasediments (Table
249 2). Given the abundance of metaradiolarites in the LT soles, the flow law of quartz is considered
250 here as representative. Felsic granulite (dashed purple curve; Fig. 4a) may represent an equivalent to
251 a strongly metamorphosed metasediment.

252 Importantly, at any given temperature and (at least as a first order approximation) regardless of
253 which flow law is used, the mechanical strength of peridotite (i.e., dry or wet olivine: thick green
254 curves and green overlay, respectively; Fig. 4a) is greater than that of mafic oceanic crust (blue
255 overlay in Fig. 4b). Sediments are weaker than basalt, yet stronger than serpentinite. This is
256 emphasized in figure 4b, where averages of flow laws are shown for the mantle (i.e., dislocation
257 creep for dry and wet olivine and diffusion creep or disGBS with a grain size of 30 μm), for the
258 mafic crust ("basalt") and for serpentinite. It is emphasized that changing the strain rate modifies the
259 absolute value of η but does not affect the relative position of these curves (see supplementary
260 figure S1). The strength contrasts existing between these different materials therefore seem
261 independent of strain rate.

262

3.2 Rheological switches across the plate interface

Slab dehydration (see Faccenda, 2014 for a review) can be anticipated to be critical for mechanical coupling during subduction infancy. Fluids released into the nascent mantle wedge (Fig. 4c) will induce serpentinization of the mantle below ~550-650°C (depending on pressure: Fig. 3a; Ulmer and Trommsdorff, 1995). These fluids will be stored in progressively lesser amounts deeper down, first as hydrous phases such as chlorite ± amphibole ± phlogopite ± talc, then at T > ~850-900°C as fluid inclusions or point defects in nominally anhydrous minerals such as olivine or pyroxene (Hirth and Kohlstedt, 2015).

Contrary to the general increase of material strength with cooling (Fig. 4b), cooling of hydrated mantle wedge peridotites will therefore progressively weaken the mantle wedge towards serpentinite rheology (from point i to f; Fig. 4b) by (i) absorption of OH in olivine ("wet" olivine) at 1000-900°C and changes in deformation mechanisms from dislocation creep to grain size sensitive creep at T < ~850-900°C (i.e., diffusion creep and disGBS), (ii) formation of weaker hydrated minerals and eventually (iii) serpentinization. Noteworthily, the viscosity of an even mildly serpentinised peridotite (> 15%) approaches that of pure serpentine (Escartin et al., 2001).

Although the exact rheological path from peridotite to serpentinite cannot be precisely quantified presently, an important conclusion is that mantle wedge viscosities will cross over the curves for metabasalt and then metasediment (Fig. 4b): these two "rheological switches" (i.e., when the mantle wedge first becomes weaker than basalts, then than sediments) most probably occur at T ~800°C (where deformation by diffusion creep and disGBS have similar effective viscosities; Figs. 4a,b) and ~600°C, respectively. The temperature and viscosity values for the HT rheological switch (Fig. 4d) both match the temperature (T~800-850°C; Boudier et al., 1988; Linckens et al., 2011a) and viscosity ($\eta \sim 10^{20\text{-}21}$ Pa.s; Linckens et al., 2011b; Tasaka et al., 2014) inferred from the high strain mylonitic to ultramylonitic deformation of adjacent banded peridotites from the base of the ophiolite.

4. Model for slab penetration into the mantle and metamorphic sole formation

4.1 Evolution of rheological contrasts across the plate interface during subduction infancy

Figure 4d shows the evolution of the rheological contrast across the plate interface during incipient slab penetration, as the top of the slab progressively heats up, weakens and dehydrates. The top of the slab is first considered as essentially made of mafic crust (i.e., basalt; Fig. 4c), sediments being probably scarce at the start of intra-oceanic subduction, far away from the continent (Fig. 1a). At shallow depths and for temperatures below ~550-600°C, the subducting oceanic (basaltic) crust is juxtaposed against an incipiently serpentinised mantle on top (as schematized in Fig. 4c). A sharp viscosity contrast ($\Delta\eta$) exists on either side of the subduction plane (strong basalt vs. weak mantle wedge; Fig. 4d).

As depth and temperature increase, the subducting crust weakens and progressively encounters a warmer, stronger, unserpentinised and less hydrated mantle wedge ($\Delta\eta'$ on Fig. 4d), where grain size sensitive deformation mechanisms take over (Linckens et al., 2011a; Hirth and Kohldstedt, 2015). The viscosity contrast across the interface reverses (weak basalt vs. stronger mantle wedge) at T > ~800°C, once the subducting crust is juxtaposed against an almost dry peridotite rheology ($\Delta\eta''$ on Fig. 4d).

A similar evolution can be envisioned if sediments are present on top of the slab, with a viscosity reversal (sediment vs. mantle wedge) taking place at ~600°C ("second rheological switch"; Fig. 4d). Although the extent to which basalts and sediments harden as a result of prograde mineral transformations is unknown, flow laws indicate that these rheological switches exist, even considering the change from basalt to mafic granulite or from sediment/quartzite to felsic granulite (Fig. 4a). They will also take place regardless of the age of the overriding lithosphere, although at different depths (the warmer the lithosphere, the shallower the rheological switches).

Rheological switches bear major consequences on mechanical coupling during early slab penetration:

316 (i) at any given time the strength of the mantle wedge will increase downwards (Fig. 4c), so
317 that the slab can be expected to face greater resistance to penetration with depth (at least until
318 mantle melting occurs);
319 (ii) as the thermal regime cools with time, the domain where serpentine is stable ("serp. front"
320 in Fig. 4c) will expand continuously downwards.
321
322 ***4.2 Metamorphic sole formation linked to strong interplate mechanical coupling***
323 Effective viscosities of the lower plate crust and upper plate mantle therefore converge and
324 switch, during subduction infancy, across restricted T windows (Fig. 4d; with P and time generally
325 ~ 1 GPa and < 2Myr, these are restricted P-T-t windows too). We propose that the detachment and
326 accretion of metamorphic soles is triggered by peaks of interplate mechanical coupling associated
327 with rheological switches, that distribute deformation over large, km-scale bands across the
328 subduction interface (e.g., Yuen et al., 1978) and localize strain further into the slab where/if a
329 sharper viscosity contrast exists (e.g., Kimura and Ludden, 1995).
330 Slab penetration and metamorphic sole formation are tentatively reconstructed in figure 5 in
331 three major steps (isotherms and depth-time trajectories are from thermo-kinematic models detailed
332 in supplementary material; Figs. S2-4):
333 (1) Plate interface mechanical strength peaks during the first rheological switch
334 (metamorphosed basalt vs. metasomatized upper mantle; Fig. 5a) at T~750-850°C, leading to the
335 formation of essentially mafic HT metamorphic soles (dot 1a, Fig. 4d). Detachment on a weaker
336 horizon within the slab probably takes place at the transition between hydrothermalized/weakened
337 basaltic layers and drier basalts below, and/or between basalts and sheeted dykes (if present),
338 accounting for the general lack of metagabbros in metamorphic soles.
339 (2) Accretion of the metasedimentary-rich LT soles takes place at lower T (and P) conditions at
340 ~550-650°C and ~0.5 GPa, after the partial exhumation of the HT sole (Fig. 5b). This corresponds
341 to the second rheological switch (dot 1b, Fig. 4d). Two different scenarios of mechanical coupling
342 can however be envisioned: (i) between the sediments and the incipiently serpentinised, weakening

343 upper mantle (option 1; Fig. 5d) or (ii) between the sediments and the base of the HT sole (option 2;
344 Fig. 5d), whose viscosity will be shifted from basalt to sediment as the sedimentary column
345 increases (blue arrow, Fig. 4b; a similar shift is expected if strain rate increases or if basalt from the
346 HT sole get hydrated by water released from sediments below). Option 2 is supported by the
347 general lack of (serpentinised) mantle between the LT and HT sole (see section 2). Option 1 implies
348 that the mantle above the LT sole is tectonically removed by the exhumation of the (more resistant)
349 HT sole and basal peridotites (Fig. 5d). Option 1 would nevertheless explain the occurrence of LT
350 soles directly beneath the mantle. Accretion of the LT sole indicates, in any case, that the
351 detachment horizon within the slab is located within the sedimentary pile.
352 The fact that HT soles are thinner than LT soles could result from larger amounts of
353 accumulated strain and later ductile thinning, from the peeling of thinner slices during the first
354 rheological switch and/or from longer duration of accretion during the LT episode.
355 (3) As the thermal regime of the subduction continues to decrease (Fig. 5c), incoming sediment
356 and basalt remain stronger than the increasingly serpentinised mantle wedge (Fig. 4d): the plate
357 interface progressively 'unzips' downwards. LT eclogites, which start forming within the
358 refrigerated subduction zone (Fig. 5c), are less likely to get mechanically coupled to the weakened
359 upper plate. This can be the reason why they are rarely exhumed (Agard et al., 2009), in agreement
360 with their location in the serpentine stability field ("no accretion" domain in figure 3a).
361
362 ***4.3 Impact of subduction cooling on interplate mechanical coupling***
363 Figure 5 highlights how cooling dramatically impacts slab penetration during subduction
364 infancy:
365 (i) The mantle wedge acts as a buttress which progressively softens with time: it only transiently
366 peels off the slab crust during the first My, thereby forming metamorphic soles, then progressively
367 loses strength with cooling/serpentinization until full decoupling;
368 (ii) Strain localizes with time in shallower decoupling horizons within the slab (Fig. 5e): accretion
369 affects the top of the mafic crust (stage a), then only the sediments on top (stage b) and, when the

plate interface becomes decoupled after a few My (stage c), accretion is restricted to shallow, near-trench infill (e.g., unmetamorphosed Hawasina units found in Oman beneath the metamorphic sole and the ophiolite; Searle and Malpas, 1980; Searle and Cox, 2002), as in present-day accretionary wedges (e.g., Nankai prism). The width of the plate interface shear zone may therefore decrease with time.

5. Discussion

The proposed mechanism for metamorphic sole formation and slab penetration (Fig. 5) explains why, through two main steps of accretion, metamorphic soles form and get accreted at remarkably similar P-T-time conditions worldwide (section 2.3) and across a transient period of subduction lifetime only (i.e., when rheological switches take place).

5.1 Uncertainties on P-T-time conditions, viscosity estimates and strain rate

5.1.1 P-T-time constraints

P-T estimates (800 ± 50°C at 1.0 ± 0.1 GPa for the early thin HT sole and 600 ± 50°C at ~0.5 ± 0.1 GPa for the late, thicker LT sole; Fig. 3) depend on the accuracy of thermodynamic models for pyroxene and amphibole. These models were considerably refined but Ti- and Fe^{3+}- substitutions in amphiboles are complex and mafic melts are notoriously difficult to model (Diener and Powell, 2012 and references therein; Green et al., 2016). Larger uncertainties on pressure conditions for LT soles arise from lesser constraints in the high-variance greenschist to epidote amphibolite fields. The major uncertainty therefore lies in the exact pressure gap between the HT and LT soles, and whether there might be a continuum in between.

Age constraints for HT and LT metamorphic soles tightly cluster within 1-2 My (Table 1; Fig. 1d). The short duration of the process and/or apparent synchronicity might be exaggerated by the fact that $^{40}Ar/^{39}Ar$ ages on amphibole may represent cooling ages for the HT soles (i.e., below 550°C), whereas age constraints for the LT sole could represent crystallization ages. But the fact

397 that the LT soles are found below the HT ones (whom underlie the mantle base of the ophiolite)
398 leaves little doubt that they were accreted afterwards. Thermo-mechanical modelling of a cooling
399 subduction zone also shows that cooling lasts no more than a few My (Duretz et al., 2015).
400
401 *5.1.2 Viscosities and strain rates*
402 One of the largest uncertainties with experimental flow laws is that they are performed at (and
403 extrapolated from) conditions orders of magnitude faster than nature (typically 10^{-4}-10^{-6} s^{-1} versus
404 10^{-12}-10^{-15} s^{-1} in nature; Burov, 2011; Hirth and Kohlstedt, 2015). Field evidence, however, suggests
405 that mafic, clinopyroxene and plagioclase bearing lithologies are ~2 orders of magnitude weaker
406 than dry peridotite at ~700-800°C (e.g., Homburg et al., 2010), in agreement with the respective
407 position of calculated flow laws (Fig. 4b,c). Viscosity estimates for the first, HT rheological switch
408 (~10^{20-21} Pa.s; Fig. 4d) are also in remarkable agreement with values deduced from natural
409 observations on strained peridotites from the (ultra)mylonitic base of the ophiolite mantle (10^{20-21}
410 Pa.s; Linckens et al., 2011b; Tasaka et al., 2014).
411 Another uncertainty comes from the simplifying assumption of considering similar strain rates
412 for estimating the viscosities of all lithologies (Fig. 4b), whereas faster strain rates can be expected
413 where strain localization takes place. Regardless of strain rate, however, "rheological switches" and
414 converging mechanical behaviour between the mantle and basalt/sediment will take place across the
415 interface: as the mantle wedge evolves progressively from dry to serpentinised, its viscosity curve is
416 bound to cross that of basalt then of sediment (Fig. 4b,d), and this order is independent of strain rate
417 (e.g., from 10^{12} to 10^{14} s^{-1}; Fig. S1). This conclusion is not modified by shear heating either, which
418 only changes the temperature field and shifts the T window of metamorphic sole formation to
419 shallower depths, but not the characteristic “S-shape” of the isotherms (Fig. S5; so does the thermal
420 state of the upper plate: Figs. S2b,c).
421 Complex feedbacks may nevertheless exist, since similar viscosities on each side will increase
422 interplate mechanical coupling, which will in turn decrease strain rates, hence probably decrease
423 shear heating (also depending on the width onto which deformation is distributed). Further testing

of this scenario using self-consistent fully coupled thermomechanical models is therefore needed, but there are major challenges:

(i) refined rheologies for sediments, variably hydrated basalts and gabbros, taking into account the influence of hydrothermal alteration, progressive metamorphic recrystallization, water loss or plagioclase content on crustal rocks are unknown (e.g., Getsinger and Hirth, 2014). The same holds true for the rheology of the mantle wedge (as yet unconstrained, as is fluid migration inside; Faccenda, 2014), for polyphase lithologies that also probably exist along the plate interface, for the impact of subordinate amounts of melt in the HT soles (<~10%), or for assessing the influence of pressure or the extent to which frictional energy is converted into heat (which also depends on rheological laws).

(ii) appropriate spatial resolution (i.e., down to ~10 m) is required in self-consistent visco-elasto-plastic geodynamic models in order to localize strain and (progressively) slice and detach pieces from the slab, in addition to reaching sufficient temporal resolution (e.g., van Dinther et al., 2014).

Further modelling will help constrain the depth and duration of these processes. The simple thermo-kinematic models used to derive the isotherms of figure 5 (see supplementary material) suggest that for a set of realistic velocities, initial thermal age and slab dip, incoming crustal rocks may cross the temperature range of HT sole formation (~750-850°C) at depths of ~25-35 km and that accretion of individual slices may last on the order of 0.3-0.4 My (Fig. S3). Although inferred from simplified models, these constraints point to the possible formation of metamorphic soles across a range of depths, possibly accounting for some of the scatter observed in the P-T estimates for metamorphic soles worldwide (Fig. 3a).

5.2 Accretion and exhumation during subduction infancy

5.2.1 Accretion of HT soles and incorporation of HT eclogites in serpentinite mélanges

Accretion of mafic HT soles will last less than shown in the reconstruction and probably stop (or decrease) once a significant amount of sediments reaches the trench and becomes involved in

451 the plate interface (Fig. 5b): since incoming sediments reach their rheological switch with the
452 mantle wedge at lower T than basalts (Figs. 4c,d), their arrival along the plate interface will indeed
453 localize strain and thus deactivate basalt accretion.

454 As a result of progressive cooling of the subduction zone, potential accretion of HT soles
455 further downdip can be predicted for a few more My after subduction initiation (Fig. 5b). Such
456 rocks, however, are not accreted below ophiolites and/or not exhumed, which could be due to rock
457 densities exceeding mantle values (thermodynamic modelling shows that this will be the case for
458 basalt at 800°C for P > 1.2 GPa), to dynamics associated with melting at depth (Faccenda, 2014)
459 and/or to the resumption of full coupling between the plates (Syracuse et al., 2010) dragging down
460 these rocks irreversibly.

461 In contrast, later and further downdip, the mantle wedge will get colder, more hydrated and
462 therefore more buoyant while transiently remaining fairly strong (i.e., still mechanically strongly
463 coupled). HT eclogites and the heterogeneously hydrated/weakened mantle wedge may thus reach
464 broadly equivalent viscosities towards the end of subduction infancy, thereby favouring mechanical
465 coupling, rock mixing and fast (buoyant) joint exhumation. This could explain the anticlockwise,
466 short-lived exhumation of HT eclogites in serpentinite mélanges at depths of 50-60 km and ~5 My
467 after subduction nucleation (Figs. 3a, 5c; e.g., Franciscan complex or Serpentinite mélange of Cuba:
468 Garcia-Casco et al., 2006).

469

470 *5.2.2 Exhumation of HT soles and basal peridotites: the depth conundrum*

471 This study highlights the contrast between the juxtaposition of HT soles and basal peridotites at
472 ~25-35 km (assuming purely lithostatic P estimates) and the final ophiolite thickness (≤10-15 km).
473 Whether this can be explained by mantle thinning (Casey and Dewey, 1984; Dewey and Casey,
474 2013) or relative exhumation (or both) has been a matter of speculation (e.g., the "conundrum of
475 Samail"; Hacker and Gnos, 1997). Mantle thinning would have to be concentrated within the basal
476 peridotites (500-1000 m thick at present) as the rest of the mantle section is mostly undeformed

(Ceuleneer et al., 1988; Nicolas et al., 2000), and does not explain how metamorphic soles get accreted.

Based on the pressure difference between the HT and LT soles and on the similar P-T conditions retrieved from HT soles and basal peridotites (e.g., Jamieson, 1981; McCaig, 1983; this study), the reconstruction of figure 5 depicts their relative exhumation with respect to the rest of the overlying oceanic lithosphere, thanks to buoyancy/rheology contrasts (and through successive stacks: HTsole\peridotite, then LTsole\HTsole\peridotite). The lower density of the slices would account for their exhumation with respect to the overlying mantle, while the rheology (viscosity) constrasts above and below the slices would favour strain localization. Relative exhumation is also supported by the existence of rare blueschist facies overprints on HT soles underlain by blueschist facies rocks (e.g., Turkey; Plunder et al., 2015, 2016), indicating that, in some cases, the HT sole is not immediately exhumed and stagnates at depth (which would not be the case if the mantle was systematically thinned).

An alternative explanation to the depth conundrum could be that the ~1 GPa pressure estimate for the HT soles corresponds to overpressure arising from strongly coupled lithologies (i.e., dry mantle against basalt; McCaig, 1983). Depths attributed to the deformation of HT soles and basal peridotites could then be reduced by up to a factor of 2 (Petrini and Podladchikov, 2000), matching both the depths/pressures of LT soles and final ophiolite thickness (~10-15 km). Whether such rocks, affected by strong ductile deformation, may sustain excess dynamic pressure is unclear and could be tested with numerical models (with limitations discussed in section 5.1.2). Overpressure would not, however, affect the conclusions of this study regarding mechanical coupling, accretion or the existence of rheological switches.

5.2.3 Are metamorphic soles formed beneath supra-subduction ophiolites?

While the proposed mechanism emphasizes the importance of rheology during subduction infancy, the nature and genesis of ophiolites is still a matter of debate (see Rioux et al., 2013 for a recent discussion), with authors in favour of a MORB-type pre-existing lithosphere (Nicolas, 1989;

Nicolas et al., 2000) and others supporting an entirely supra-subduction origin (Stern and Bloomer, 1992). In the first hypothesis, formation of oceanic lithosphere shortly predates intra-oceanic subduction (via near-ridge, detachment or transform fault inversion; Boudier et al., 1988), while in the second hypothesis intra-oceanic spontaneous subduction (often assumed to take place at transform faults) triggers the formation of supra-subduction lithosphere by mantle upwelling (e.g., Stern and Bloomer, 1992). The interplay between lithology/rheology, T (and P) and mechanical coupling of our proposed mechanism could in principle operate through either inversion of small oceanic basins or mantle upwelling following spontaneous subduction initiation. The second scenario, however, less easily explains the systematic juxtaposition of HT soles onto LT soles (and the sharp lithological divide between them), as well as the slightly younger and more dispersed ages of the metamorphic soles when compared to those of the ophiolite crust (Fig. 1d; Wakabayashi and Dilek, 2000, 2003). Metamorphic sole formation may thus question the popular spontaneous subduction initiation model (Stern and Bloomer, 1992).

5.3 Rheological implications

An important inference from this model is that the effective rheologies of the mantle and crust are similar at ~800°C and ~1 GPa in the presence of fluids. This is an important anchor point for experimental rock mechanics, supporting the validity of extrapolations from laboratory experiments performed orders of magnitude faster than in nature. Although the viscosity-temperature path of the mantle wedge (from i to f; Fig. 4b) or location of the first rheological switch are not determined with precision yet, their location (at ± 50°C and ~1 order of magnitude in viscosity) further supports the convergence of the experimental grain size dependent flow laws at ~800°C (i.e., at the temperature of HT sole formation; Fig. 4d).

Figure 5 also highlights the importance, for strain localization during subduction infancy, of lubrication by hydrous phases (Regenauer-Lieb et al., 2001; Dymkova and Gerya, 2013) and grain size reduction (Linckens et al., 2011b; Hirth and Kohldstedt, 2015). Viscosity estimates for sole formation (Fig. 4d) match those inferred for the nucleation of throughgoing low viscosity shear

zones (~10^{20} Pa.s; Regenauer-Lieb et al., 2001). Although mantle wedge rheology likely depends on the extent of serpentinization and higher T ductile deformation, the similarity of ophiolite soles worldwide suggests that regional variations (e.g., incoming material, convergence rates, effective fluid release) are averaged out.

The presence of a warm oceanic lithosphere (i.e., <~3 My and/or rejuvenated; Hacker, 1990; Duretz et al., 2015; supplementary material) appears to be an important requirement for metamorphic sole formation. Their formation is probably inhibited for older lithospheres, not because they are too cold (warm conditions will be met deeper down) but because the plate interface will be too decoupled. On the other hand, previous studies suggested that one-sided intraoceanic subduction initiation requires significant mantle cooling and subsequent weakening (Crameri et al., 2012). Too strong mechanical coupling, during subduction infancy, would favour double-sided subduction as in the Archean (Sizova et al., 2010 and references therein). This potentially explains why ophiolite soles older than the Neo-proterozoic are missing.

These findings also bear important implications for mechanisms of sediment or seamount underplating (i.e., transient episodes of strong coupling may control, in long-lived subduction systems, the potential accretion/exhumation of HP-LT rocks, including eclogites; Kimura and Ludden, 1995; Agard et al., 2007), variably hydrated mantle wedge rheologies (Faccenda, 2014) and for geochemical budgets of volatile fluxing during (hot) subduction (Ishikawa et al., 2005; Sizova et al., 2010).

6. Conclusions

Combining structure-lithology-P-T-time data from metamorphic soles with flow laws derived from experimental rock mechanics, we herein (i) outline the existence of two major, systematic rheological switches across the subduction interface (mantle wedge vs. basalts, then mantle wedge vs. sediments), (ii) propose that they control slab penetration and the successive formation of HT

then LT metamorphic soles and (iii) provide a tentative reconstruction of metamorphic sole accretion during subduction infancy.

This reconstruction provides a generic explanation for the ubiquitous formation of metamorphic soles and emphasizes how slab progression is hindered, during subduction infancy, by progressive changes in the mechanical properties of the cooling plate interface, until the interface becomes fully decoupled. Metamorphic sole formation and accretion would not so much result from a transient HT event (i.e., an 'ironing' effect), but from the existence of transiently similar rheologies and strong coupling during subduction infancy.

This study sheds light on early slab dynamics and on the role of transient mechanical coupling along the plate interface (i.e., such transient episodes may also control accretion/exhumation of HP-LT rocks in mature subduction systems) and provides a testable hypothesis for thermo-mechanical models. The proposed mechanism also strengthens the applicability of experimentally-derived flow laws for the mantle and mafic crust: although calibrated at much higher strain rates, they appear to be in remarkable agreement with natural data at ~800°C (and ~1 GPa).

Acknowledgements

This work was funded through the Agence nationale de la recherche (ANR-10-BLAN-0615) and through Institut Universitaire de France (grant to P.A.). We are grateful to colleagues from the O:NLAP ANR project for fruitful and enthusiastic discussions. An earlier version of this manuscript benefited from the constructive remarks of our friend and colleague E. Burov, who sadly passed away, and A. Schubnel. This work also benefited from discussions with scientists from the ZIP project (REA grant agreement no. 604713 (ZIP "Zooming In between Plates") from the People Programme (Marie Curie Actions) of the European Union's Seventh Framework Programme FP7/2007-2013).

585

586 **REFERENCES**

587

588 Agard, P., Jolivet, L., Vrielynck, B., Burov, E., Monie, P., 2007. Plate acceleration: The obduction
589 trigger? Earth Planet. Sci. Letters 258, 428–441.
590 Agard et al., Agard, P., Yamato, P., Jolivet, L. & Burov, E. 2009. Exhumation of oceanic blueschists
591 amd eclogites in subduction zones: Timing and mechanisms. Earth-Sci. Rev. 92, 53-79.
592 Baldwin, J.A., Powell, R., Brown, M., Moraes, R. and Fuck, R.A., 2005. Modelling of mineral
593 equilibria in ultrahigh-temperature metamorphic rocks from the Anápolis–Itaucu Complex,
594 central Brazil. J. Metamorph. Geol., 23, p. 511–531.
595 Boudier, F., Ceuleneer, G. & Nicolas, A. 1988. Shear zones, thrusts and related magmatism in the
596 Oman ophiolite : Initiation of thrusting on an oceanic ridge. Tectonophysics 151, 275-296.
597 Casey, J. F. & Dewey, J. 1984, Initiation of subduction zones along transform and accreting plate
598 boundaries, triple-junction evolution, and forearc spreading centres: implications for
599 ophiolitic geology and obduction Geol. Soc. Lond. Spec. Pub. 13, 269-290.
600 Çelik, Ö.F., Marzoli, A., Marschik, R., Chiaradia, M., Neubauer, F. and Öz, I., 2011. Early–Middle
601 Jurassic intra-oceanic subduction in the İzmir-Ankara-Erzincan Ocean, Northern Turkey:
602 Tectonophysics, 509, p. 120–134, doi: 10.1016/j.tecto.2011.06.007.
603 Ceuleneer, G., Nicolas, A. and Boudier, F., 1988. Mantle flow patterns at an oceanic spreading
604 centre: the Oman peridotites record. Tectonophysics 151, 1-26.
605 Coleman, R.G., 1981. Tectonic setting for ophiolite obduction in Oman. J. Geophys. Res. 86, 2497-
606 2508.
607 Crameri, F., Tackley, P. J., Meilick, I., Gerya T. & Kaus, B. J. P. 2012. A free plate surface and weak
608 oceanic crust produce single-sided subduction on Earth. Geophys. Res. Lett. 39, L03306.
609 de Capitani, C. & Petrakakis, K. 2010. The computation of equilibrium assemblage diagrams with
610 Theriak/Domino software. Am. Mineral. 95, 1006–1016.
611 Dewey, J. 1976. Ophiolite obduction. Tectonophysics. 31, 93-120.
612 Dewey, J.F. and Casey, J.F., 2013. The sole of an ophiolite: the Ordovician Bay of Islands Complex,
613 Newfoundland: Journal of the Geological Society, London, 170, p. 715–722, doi:
614 10.1144/jgs2013-017.
615 Diener, J.F.A., Powell, R., White, R.W. and Holland, T.J.B., 2007. A new thermodynamic model for
616 clino- and orthoamphiboles in the system Na2O-CaO-FeO-MgO-Al2O3-SiO2-H2O-O. J.
617 Metamorph. Geol., 25, p. 631–656, doi: 10.1111/j.1525-1314.2007.00720.x.
618 Diener, J. F. A. & Powell, R. 2012. Revised activity–composition models for clinopyroxene and
619 amphibole. J. Metamorph. Geol. 30, 131-142.

620 Duretz, T., Agard, P., Yamato, P., Ducassou, C., Burov, E.B., Gerya, T.V. 2015. Thermo-mechanical
621 modeling of the obduction process based on the Oman Ophiolite case, Gondwana Research,
622 doi:10.1016/j.gr.2015.02.002.
623 Escartin, J., Hirth, G. & Evans, B. W. 2001. Strength of slightly serpentinised peridotites:
624 implications for the tectonics of oceanic lithosphere, Geology 29, 1023–1026.
625 Faccenda, M. 2014. Water in the slab: A trilogy, Tectonophysics 614, 1-30.
626 Faul, U. H., Jackson, I. 2007. Diffusion creep of dry, melt-free olivine, J. Geophys. Res., 112,
627 B04204, doi:10.1029/2006JB004586.
628 García-Casco, A., Torres-Roldán, R. L., Iturralde-Vinent, M., Millán, G., Cambra, K. N., Calisalvo,
629 C. L., & Vega, A. R. 2006. High pressure metamorphism of ophiolites in Cuba. Geol. Acta 4,
630 63-88.
631 Getsinger, A. J. & Hirth, G. 2014. Amphibole fabric formation during diffusion creep and the
632 rheology of shear zones. Geology 42, 535-538.
633 Gnos, E. 1998. Peak Metamorphic Conditions of Garnet Amphibolites Beneath the Semail
634 Ophiolite: Implications for an Inverted Pressure Gradient. Int. Geol. Rev. 40, 281-304.
635 Green, E. C. R., White, R. W., Diener, J. F. A., Powell, R., Holland, T. J. B., Palin, R. M., 2016.
636 Activity–composition relations for the calculation of partial melting equilibria for metabasic
637 rocks. J. Metamorph. Geol., accepted for publication.
638 Gurnis, M., Hall, C. & Lavier, L. 2004. Evolving force balance during incipient subduction.
639 Geochem, Geophys. Geosyst. 5, Q07001.
640 Hacker, B.R., 1990. Simulation of the Metamorphic and Deformational History of the Metamorphic
641 Sole of the Oman Ophiolite, J. Geophys. Res., 95, 4895-4907.
642 Hacker, B. R., Mosenfelder, J. L. & Gnos, E. 1996. Rapid emplacement of the Oman ophiolite:
643 Thermal and geochronologic constraints. Tectonics. 15, 1230-1247.
644 Hacker, B. R. & Gnos, E. 1997. The conundrum of samail: explaining the metamorphic history.
645 Tectonophysics 279, 215-226.
646 Hansen, L.N., Zimmerman, M.E., Kohlstedt, D.L., 2011. Grain boundary sliding in San Carlos
647 olivine: flow law parameters and crystallographic-preferred orientation. J. Geophys. Res.116,
648 B08201.
649 Hilairet, N., Reynard, B., Wang, Y., Daniel, I., Merkel, S., Nishiyama, N., Petitgirard, S. 2007.
650 High-pressure creep of serpentine, interseismic deformation and initiation of subduction.
651 Science. 318, 1910-1913.
652 Hirth, G., Kohlstedt, D.L., 2003. Rheology of the upper mantle and the mantle wedge: a view from
653 the experimentalists. In: Inside the Sub-duction Factory (Ed. Eiler, J.), Geophys. Monogr. 138,,
654 American Geophysical Union, Washington, D.C., 83–105.

Hirth, G. & Kohlstedt, D. L. 2015. The stress dependence of olivine creep rate: Implications for extrapolation of lab data and interpretation of recrystallized grain size. Earth Planet. Sci. Lett. 418, 20-26.

Holland, T.J.B. & Powell, R. 1998. An internally consistent thermodynamic data set for phases of petrological interest. J. Metamorph. Geol. 16, 309-343.

Homburg, J.M., Hirth, G., Kelemen, P.B. 2010. Investigation of the strength contrast at the Moho: A case study from the Oman Ophiolite, Geology, 38, 679-682.

Ishikawa, T., Fujisawa, S., Nagaihi, K. & Masuda T. 2005. Trace element characteristics of the fluid liberated from amphibolite-facies slab: Inference from the metamorphic sole beneath the Oman ophiolite and implication for boninite genesis. Earth Planet. Sci. Lett. 240, 355-377.

Jamieson, R. A. 1981. Metamorphism during ophiolite emplacement—the petrology of the St Anthony Complex, J. Petrol. 22, 397-443.

Jamieson, R. A. 1986. P-T paths from high temperature shear zones beneath ophiolites. J. Metam. Geol 4, 3-22.

Karato, S. 2010. Rheology of the Earth's mantle: A historical review, Gondwana Research, 18, 17–45.

Kimura, G. & Ludden, J. 1995. Peeling oceanic crust in subduction zones. Geology 23, 217-220.

Linckens, J., Herwegh, M. & Müntener, O. 2011. Linking temperature estimates and microstructures in deformed polymineralic mantle rocks. Geochem, Geophys. Geosyst. 12, Q08004.

Linckens, J., M. Herwegh, O. Müntener, and I. Mercolli (2011), Evolution of a polymineralic mantle shear zone and the role of second phases on the localization of deforma- tion, J. Geophys. Res., 116, B06210, doi:10.1029/ 2010JB008119.

McCaig, A. M. 1983. P−T conditions during emplacement of the Bay of Islands ophiolite complex. Earth Planet. Sci. Lett. 63, 459-473.

Michibayashi, K., Mainprice, D. 2004. The role of pre-existing mechanical anisotropy on shear zone development within oceanic mantle lithosphere: an example from the Oman ophiolite. J. Petrol., 45, 405-414.

Nicolas, A., 1989. Structures in Ophiolites and Dynamics of Oceanic Lithosphere (Petrology and Structural Geology). Kluwer, Dordrecht.

Nicolas, A., Boudier, F., Ildefonse, B., Ball, E., 2000. Accretion of Oman and United Arab Emirates ophiolite - Discussion of a new structural map. Mar. Geophys. Res., 21, 147-179.

Petrini K, & Podladchikov Y. 2000. Lithospheric pressure-depth relationship in compressive regions of thickened crust. J. Metamorph. Geol., 18, 67-77.

689 Plunder, A., Agard, P., Chopin, C., Pourteau, A., & Okay, A. I. 2015. Accretion, underplating and
690 exhumation along a subduction interface: From subduction initiation to continental
691 subduction (Tavşanlı zone, W. Turkey). Lithos 226, 233-254.
692 Plunder, A., Agard, P., Chopin, C., Soret, M., Okay, A.I., & Whitechurch, H. 2016. Metamorphic
693 sole formation, emplacement and blueschist-facies overprint: early subduction dynamics
694 witnessed by western Turkey ophiolites. Terra Nova, in press.
695 Regenauer-Lieb, K., Yuen, D. A. & Branlund, J. 2001. The Initiation of Subduction: Criticality by
696 Addition of Water? Science 294, 578-580.
697 Rioux, M. et al.. 2013. Tectonic development of the Samail ophiolite : High-precision U–Pb zircon
698 geochronology and Sm–Nd isotopic constraints on crustal growth and emplacement. J.
699 Geophys. Res. 118, 2085-2101.
700 Roberts, N.M.W., Thomas, R.J., Jacobs, J., 2016. Geochronological constraints on the metamorphic
701 sole of the Semail ophiolite in the United Arab Emirates. Geoscience Frontiers, in press.
702 Searle, M. P. & Malpas, J. 1980. Petrochemistry and origin of sub-ophiolitic metamorphic and
703 related rocks in the Oman Mountains. J. Geol. Soc. 139, 235-248.
704 Sizova, E., Gerya, T., Brown, M. & Perchuk, L. L. 2010. Subduction styles in the Precambrian:
705 Insight from numerical experiments. Lithos 116, 209-229.
706 Spray, J. G. 1984. Possible causes and consequences of upper mantle decoupling and ophiolite
707 displacement Geol. Soc. Lond. Spec. Pub. 13, 255-268.
708 Stern, R., J. & Bloomer, S. 1992. Subduction zone infancy: examples from the Eocene Izu-Bonin-
709 Mariana and Jurassic California arcs. Geol. Soc. of Am. Bull. 104, 1621-1636.
710 Stern, R. J. 2004. Subduction initiation: spontaneous and induced. Earth Planet. Sc. Lett. 226, 275-
711 292.
712 Syracuse, E. M., van Keken, P. E. & Abers, G. A. 2010. The global range of subduction zone
713 thermal models. Phys. Earth Planet. Int. 183, 73-90.
714 Tasaka, M., Hiraga, T., Michibayashi, K. 2014. Influence of mineral fraction on the rheological
715 properties of forsterite+enstatite during grain size sensitive creep: 3. Application of grain
716 growth and flow laws on peridotite ultramylonite, J. Geophys. Res. Solid Earth, 119, 840–
717 857, doi:10.1002/2013JB010619.
718 Ulmer, P., & Trommsdorff, V. Serpentine stability to mantle depths and subduction-related
719 magmatism. Science 268, 858-861 (1995).
720 Wakabayashi, J., and Dilek, Y., 2000, Spatial and temporal relationships between ophiolites and
721 their metamorphic soles: A test of models of forearc ophiolite genesis, in Dilek, Y., Moores,
722 E.M., Elthon, D., and Nicolas, A., eds., Ophiolites and Oceanic Crust: New Insights from
723 Field Studies and the Ocean Drilling Program: Boulder, Colorado, Geological Society of
724 America Special Paper 349, p. 53–64.

Wakabayashi, J. & Dilek, Y. 2003. What constitutes «emplacement of an ophiolite ?: Mechanisms and relationship to subduction initiation and formation of metamorphic soles. Geol. Soc. Lond. Spec. Pub. 218, 427-447.

White, R.W., Powell, R. and Holland, T.J.B., 2007. Progress relating to calculation of partial melting equilibria for metapelites. J. Metamorph. Geol., 25, p. 511–527, doi: 10.1111/j.1525-1314.2007.00711.x.

Williams, Smyth, W. R., 1973. Metamorphic aureoles beneath ophiolite suites and Alpine peridotites: tectonic implications with west Newfoundland examples. Am. J. Sci. 273, 594-621.

Yuen, D.A., Fleitout, L., Schubert, G., Froidevaux, C., 1978. Shear deformation zones along major transform faults and subducting slabs. Geophys. J. R. Astr. Soc. 54,93-119.

Fig. 1

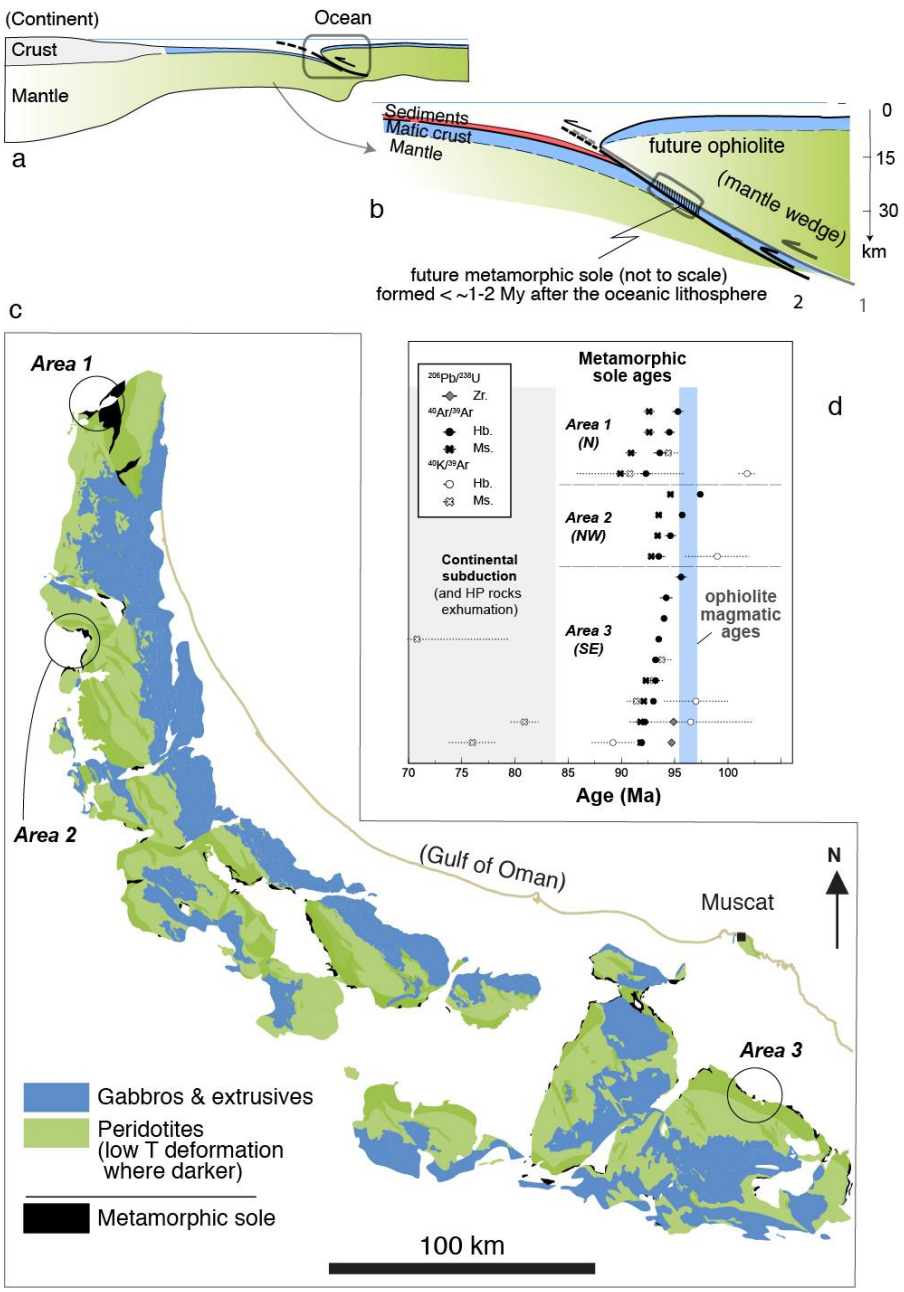


Figure 1

(a) Geodynamic setting of metamorphic sole formation during subduction infancy, following intra-oceanic subduction initiation. The later geodynamic evolution will lead to continental subduction and obduction s.s. (i.e., emplacement of the oceanic lithosphere onto continental lithosphere; after Agard et al., 2007); (b) Close-up view of Fig. 1a: the formation and accretion of metamorphic soles imply a shift of the subduction interface during subduction initiation (from thrust 1 to thrust 2); (c) simplified geological map highlighting the striking continuity of the metamorphic sole beneath the mantle of the Oman ophiolite (modified after Nicolas et al., 2000); (d) age constraints for metamorphic sole formation along the Oman ophiolite (Hb: hornblende; Ms: white mica; Zr: zircon; see Table 1 for references). Radiometric ages for the ophiolite are shown for comparison (after Rioux et al., 2013; see discussion in section 5.2).

#	Reference Location	Authors	Thickness (m) HT	LT	High temperature conditions *P* (GPa)	*dP* (GPa)	*T* (°C)	*dT* (°C)	t (Ma)	Low temperature conditions** *P* (GPa)	*dP* (GPa)	*T* (°C)	*dT* (°C)
		Gnos, 1998	≤ 70		1.1	0.2	800	100	95	0.5	0.05		
		Gnos and Kurz, 1994	2000		0.77	0.12	825	25					
		Ghent and Stout, 1981	30-40	80-85	0.5	0.2	810	55					
		Hacker and Mosenfelder, 1996					825		92.6–95.7				
		Hacker and Gnos, 1997					825	50					
		Searle and Cox, 2002			1.16	0.16	840	70					
1	**Oman**	Searle and Malpas, 1980			0.5?		825	50					
		Bucher, 1980								0.4	0.1	500	50
		Hacker et al., 1997							93.7 ± 0.8				
		Hacker et al., 1996	≤ 500						92.6–95.7				
		Hacker, 1994							92.4–95.7				
		Warren et al., 2003							94.5 ± 0.23				
		Cowan et al., 2014	80	150	1.2	0.1	840	60					
		Okay et al., 1998			0.85	0.35	700	50					
		Plunder et al., 2015			1.1	0.2	800	60					
		Dilek and Whitney, 1997	10–150				≥ 560		92–90				
2	**Turkey**	Önen and Hall, 1993	35	122	0.3	0.1	750	50	93–90				
		Önen, 2003							92–90				
		Parlak and Delaloye, 1999							92.6 ± 0.2				
		Celik and Delaloye, 2006	≤500						91.2 ± 2.3	0.55	0.05	575	25
3	**Caucasus**	Hassig et al., 2013							91–94				
		Hassig et al., 2015			0.65	0.05	≥ 630		90.8 ± 3				
4	**Dinarides**	Pamic et al., 2002	≤600		0.83	0.1	710	40	136 ± 15				
		Gaggero et al., 2009	600		0.7		730	110	162.4–172.6	0.6	0.1	624	9
5	**Cyclades**	Gartzos et al., 2009	≤250						150–155				
	Greece	Saccani and Photiades, 2004							163 ± 3–172 ± 5				
6	**Syria**	Al-Ryami et al., 2002	200–300				≥ 600						
		Parlak et al., 1996							93.4 ± 2				
7	**Egypt**	El-Naby et al., 2000			0.75	0.15	700		630–590	0.62	0.15	550	80
		Farahat, 2011			0.6	0.15	670	50					
		Malpas, 1979	70				750	50		0.6	2	625	75
		Jamieson, 1981			0.85	0.15	875	25	480 ± 5	0.42	0.07	600	50
8	**Newfoundland**	Mc Caig, 1983	70	80	0.9	0.2	800	50	477 ± 5				
		Jamieson, 1986			0.8	0.25	900	50		0.4	0.1	575	75
		Savic, 1988	100		0.75	0.15	750	100					
		O'Beirne-Ryan et al., 1990			0.85	0.05	800	50					
		Trzcienski, 1988	50	450	1.2		840						
9	**Québec**	Clague et al., 1981			0.65	0.15	775	35					
		Malo et al., 2008							465.2 ± 2				
10	**Brooks Range**	Harris, 1998	500		0.5		≥ 650		164–169				
11	**California**	Wakabayashi, 1990			0.95	0.05	645	15	160–163				
12	**Cuba**	Lazarro et al., 2013			0.86	0.01	655	10	70				
13	**Tibet**	Guilmette et al., 2015			1.2	0.25	850	100	132–127				
14	**Philippines**	Encarnacion et al., 1995	80–250		0.95		730	30	34 ± 0.6				
15	**Sulawesi**	Parkinson, 1998	300	300			700	60	30	0.5	0.1	555	15
16	**Australia**	Meffre et al., 2012			0.85	0.15	725	25	511 ± 4				
17	**New Caledonia**	Cluzel et al., 2012			0.6	0.3	800	100	55 ± 2				
18	**Papua**	Lus et al., 2004	40	160	0.4		900		58.3 ± 0.4				
	THIS STUDY												
	Oman (Kh)	This study	100	200	0.95	0.1	850	30					
	Oman (Sum)	"	35	300	0.75	0.1	810	25					
	Turkey (Yes)	"	10	100	1.05	0.15	790	35					
	Turkey (Küt)	"	5	20	1.0	0.15	800	40					

Table 1

Worldwide compilation of data on metamorphic soles (temperature, pressure, metamorphic ages and thicknesses; **: estimates from amphibole-plagioclase thermometry, amphibole barometry or other methods). See supplementary material for references. Abbreviations: Kh: Khubakhib; Küt: Kütahya; Sum: Sumeini; Yes: Yesilova).

Fig. 2

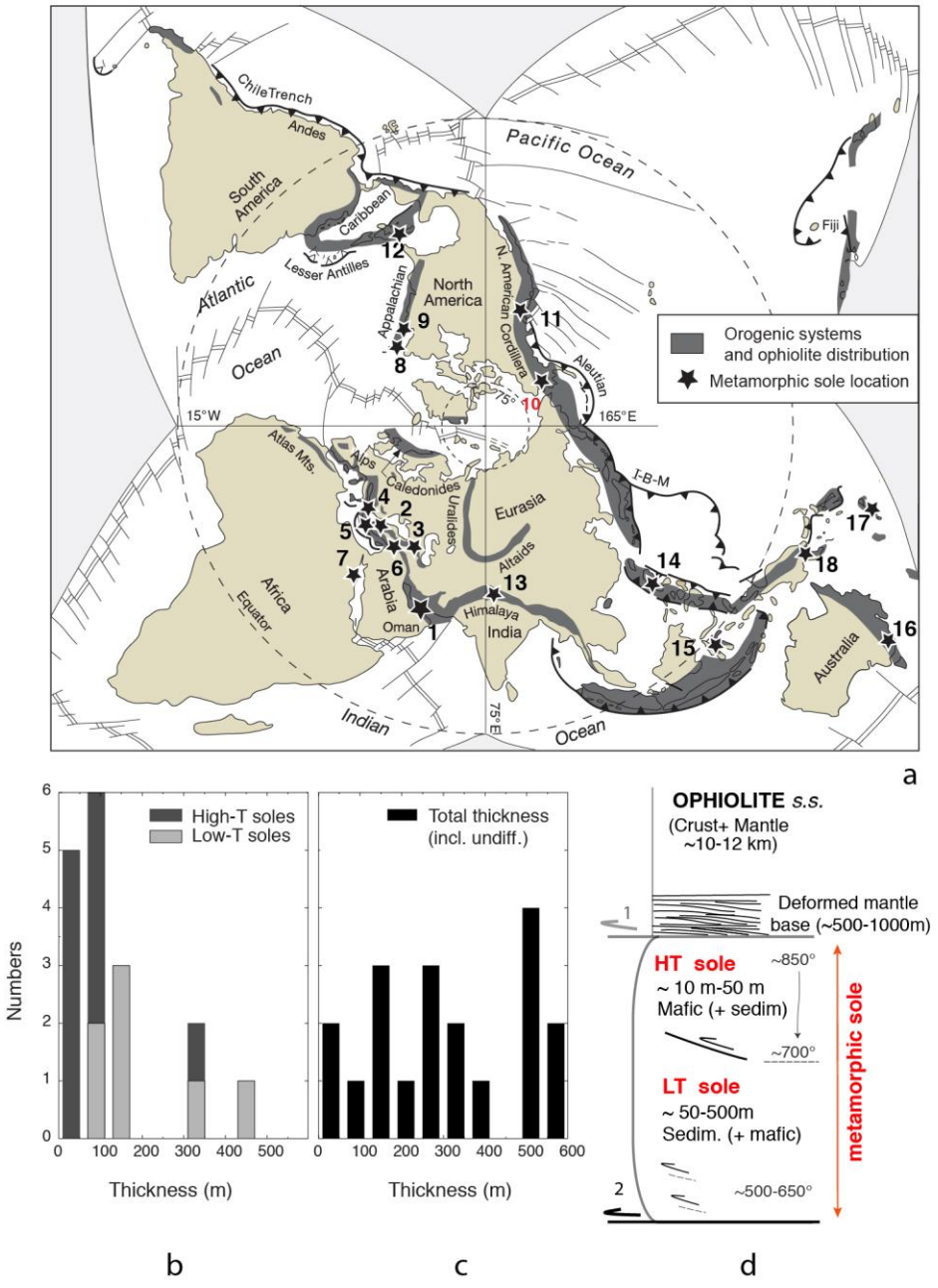


Figure 2

(a) Location of metamorphic soles and of the main large-scale obducted ophiolites worldwide (spanning late Proterozoic to Phanerozoic times); (b) and (c): histograms of thicknesses for metamorphic soles (after Table 1); (d) general structure of ophiolite soles (not to scale), emphasizing differences between the HT and LT sections. (temperature indications after Fig. 3a). Note the strongly deformed mantle section at the base of the ophiolite. Thrusts 1 and 2 as in figure 1b.

Fig. 3

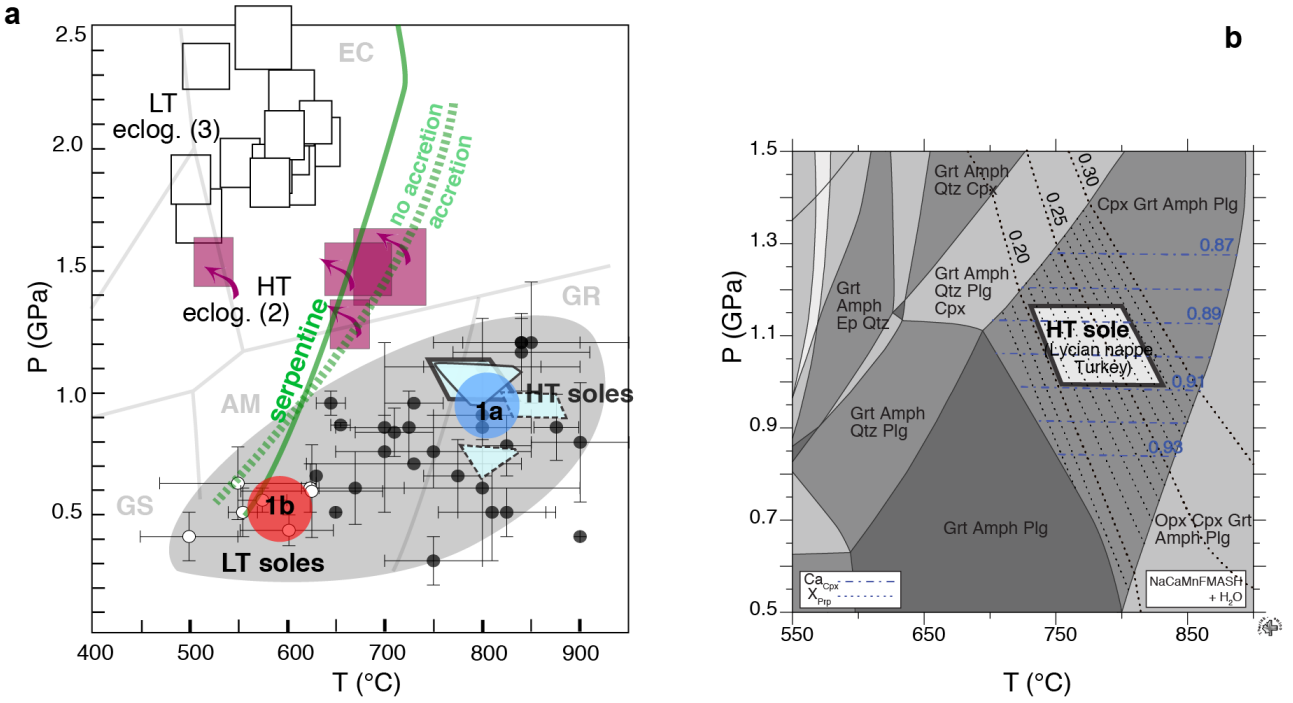


Figure 3

(a) Compilation of pressure-temperature data for HT (black) and LT (white) metamorphic soles (see Table 1; all are enclosed in the grey shaded area). P-T conditions for representative eclogites (HT: purple; LT: white) are also given for comparison (after Agard et al., 2009). Arrows outline counterclockwise P-T paths for HT eclogites. Boxes in the HT sole domain correspond to phase diagram calculations in this study. Plain boxes: results for two sample locations in Turkey (Kütahya and Yesilova); dashed boxes: results for two locations in Oman (Sumeini and Khubakhib). The diamond-shaped box with a thicker contour correponds to the estimate for the HT sole sample from Yesilova described in the text and in figure 3b. Samples have the following molar proportions (%): Kutahya: Si (46.92), Al (16.14), Fe (9.98), Mg (10.08), Ca (10.49), Na (6.39) / Yesilova: Si (44.29), Al (16.77), Fe (7.68), Mn (0.45), Mg (15.52), Ca (10.37), Na (4.14)/ Sumeini: Si(43.24) Al(15.66) Fe(10.46) Mg(11.37) Ca(16.81) Na(2.46) / Khubakhib: Si(44.85) Al (15.67) Fe(8.82) Mg(11.51) Ca (14.36) Na (4.79). (b) Phase diagram calculated in the Na_2O–CaO–MnO–FeO–MgO–Al_2O_3–SiO_2–H_2O chemical system for a MORB-type HT metamorphic sole (YE1302b; Lycian ophiolite, W. Turkey). The studied equilibrium peak assemblage (i.e. garnet–clinopyroxene–amphibole–plagioclase) is stable within a P-T field refined using mineral isopleths (e.g., pyrope content in garnet: X_{Prp}; Calcic component in clinopyroxene: Ca_{Cpx}) to 1.08 ± 0.1 GPa and 780 ± 40 °C. Abbreviations for minerals with solid solutions: Amph: amphibole; Cpx: clinopyroxene; Ep: epidote; Grt: garnet; Opx: orthopyroxene; Plg: plagioclase; Qtz: quartz.

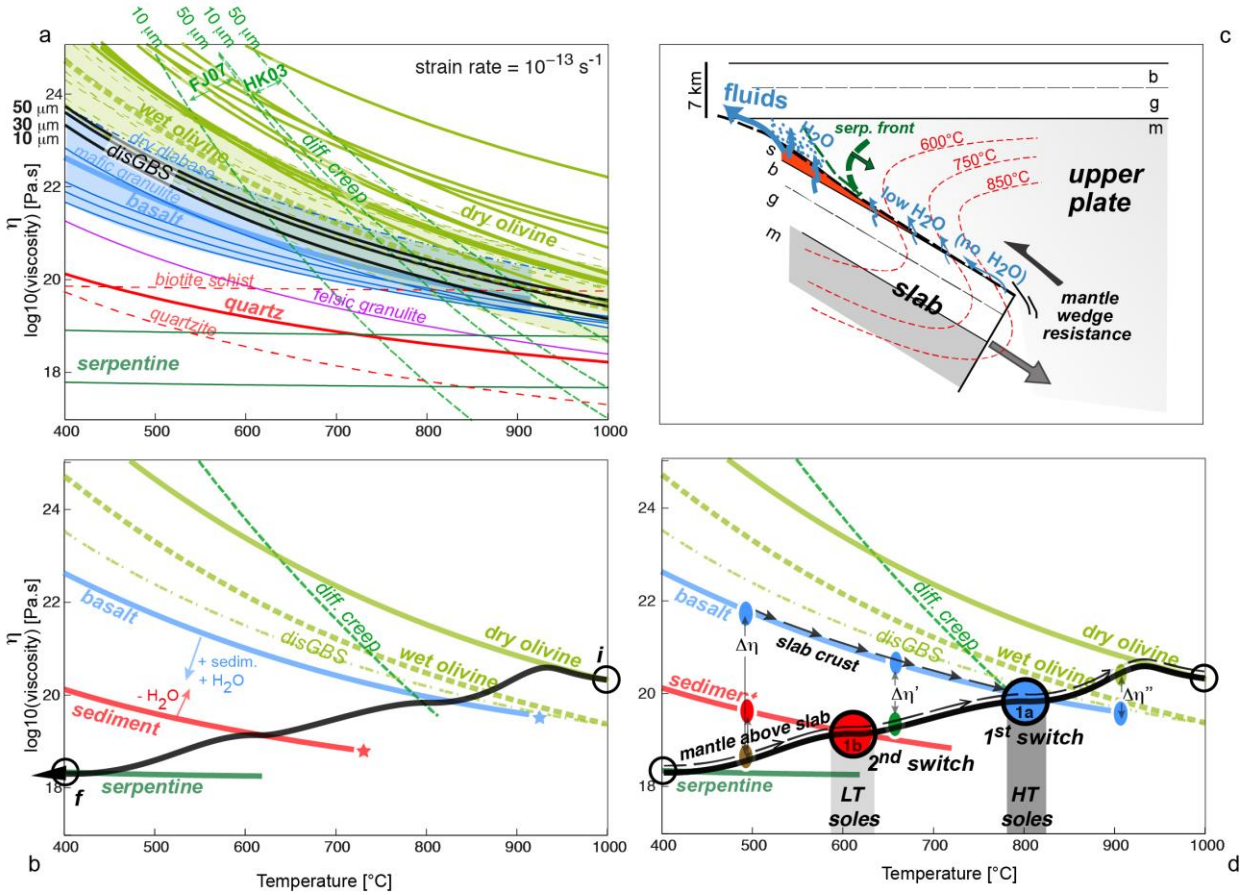


Figure 4

(a) Calculated temperature dependency of effective viscosities (η) for key plate interface lithologies (peridotite, basalt, sediments and serpentine; see Table 2 and section 3.1 for details) for an average strain rate of 10^{-13} s^{-1} (after the Oman example; Linckens et al., 2011b). Note the systematic location of the dry and wet olivine dislocation creep flow laws above those for mafic rocks (i.e., basalt, blue overlay). Abbreviations: disGBS: dislocation-accommodated grain boundary sliding; diff creep: diffusion creep; FJ07: Faul and Jackson, 2007; HK03: Hirth and Kohlstedt, 2003. Diffusion creep flow laws have been calculated for two different olivine aggregate grain sizes (10 and 50 µm) corresponding to the extreme values estimated by Linckens et al. (2011b) in Oman mantle ultramylonites.

(b) Plot of averages of published flow laws (after Fig. 4a) showing the qualitative viscosity decrease of a cooling and hydrating mantle wedge, from i to f (see text). Note that the viscosity of incoming crust will tend to decrease (from basalt to sediment) with increasing amounts of sediments and/or with addition of water released from progressive sediment dehydration. Stars mark the inception of melting of basalt and sediments (after Kessel et al., 2005 and White et al., 2007, respectively).

(c) 2D sketch of slab penetration during subduction infancy, emphasizing the importance of fluid liberation from the slab. The dashed green line bounds the stability field of serpentine ("serp. front"; blue dots suggest that only part of this domain may be effectively hydrated). Fluid storage capacity of the mantle wedge decreases downwards (see section 3.2). Background isotherms are taken after 1 My from thermo-kinematic modelling (see supplementary material). Abbreviations: s: sediments (shown here in red, as in Fig. 1b), b: basaltic layer, g: gabbroic layer, m: mantle, serp.: serpentinite;

(d) Black arrows outline evolving rheologies of the crust on top of the slab (basalt, then sediment) and of the mantle immediately above the slab (Fig. 4c) when the slab descends during subduction infancy. The rheological contrast across the plate interface between the basaltic crust and mantle wedge evolves from Δη to Δη' and Δη". Evolution along the black arrows shows the existence of two rheological switches during subduction infancy, when slab crustal rocks reach viscosities comparable to that of the mantle wedge (dots 1a and 1b; see also Fig. 3a). The temperature range for the formation of HT and LT soles is indicated.

Lithology	Authors	n	A	Q	m
			$(MPa^{-n})*(s^{-1})$	(kJ/mol)	
Slab crust					
Sediments					
Quartz	Ranalli and Murphy, 1987	3	6.80E-06	156	
Wet quartzite	Kirby and Kronenberg,1987	2.3	3.20E-04	154	
Biotite schist	Kronenberg et al., 1990	18	1.20E-30	51	
Schists	Shea and Kronenberg, 1993	31	1.30E-67	98	
Felsic granulite	Wilks and Carter, 1990	3.1	8.00E-03	243	
Mafic crust					
Basalt	Shelton and Tullis, 1981 and Hacker and Christie, 1990	3.5	1.00E-04	250	
Wet diabase	Shelton and Tullis, 1981	3.4	2.00E+04	260	
Dry diabase	Mackwell et al., 1998	4.7	8.00E+00	485	
Diabase	Van Hunen and Van den Berg, 2008	3.4	2.21E-04	260	
Microgabbro	Wilks and Carter, 1990	3.5	4.85E+04	535	
Mafic granulite	Wilks and Carter, 1990	4.2	1.40E+04	445	
Mantle wedge					
Dry olivine	Chopra and Paterson, 1981	3.6	4.50E+00	535	
"	Chopra and Paterson, 1984	3	1.00E+04	520	
“	Chopra and Paterson, 1984	3.5	2.50E-04	532	
“	Karato et al., 1986	3.5	5.40E+00	540	
“	Karato and Wu, 1993	3.5	2.42E+05	554	
“	Karato and Rubie, 1997	3	2.40E+05	554	
“	Bussod et al., 1993	3.5	1.12E+05	545	
“	Hirth and Kohlstedt, 2003	3.5	1.10E+05	548	
“	Karato and Jung, 2003	3	1.26E+06	524	
“	Li et al., 2006	3	4.57E+03	554	
“	Kawazoe et al., 2009	3.5	1.10E+05	550	
Diffusion creep	Hirth and Kohlstedt, 2003	1	1.5E+09	375	3
Diffusion creep	Faul and Jackson, 2007	1.4	2E+10	484	2
DisGBS	Hirth and Kohlstedt, 2003	3.5	6.5E+03	400	2
Wet olivine	Chopra and Paterson, 1981	4.4	2.76E+02	498	
“	Chopra and Paterson, 1981	4	2.00E+03	471	
“	Karato et al., 1986	3	1.50E+06	250	
“	Evans and Kohlstedt, 1995	4.5	2.60E+00	498	
“	Hirth and Kohlstedt, 1996	3.5	4.88E+06	515	
“	Mei and Kohlstedt, 2000	3	4.57E+03	470	
“	Mei and Kohlstedt, 2000	3	5.01E+02	508	
“	Karato and Jung, 2003	3	3.63E+00	421	
“	Karato and Jung, 2003	3	7.94E+02	470	
“	Hirth and Kohlstedt, 2003	3.5	9.00E+01	491	
“	Hirth and Kohlstedt, 2003	3.5	1.60E+03	520	
“	Mc Donnell et al., 1999*	2.14	9.10E+03	302	3
Serpentinite	Hilairet et al., 2007	5.8	2.51E-13	20.8	
"	Hilairet et al., 2007	3.8	2.51E-09	12.1	

Table 2

Published flow laws and material creep parameters used to compute the curves of figure 4b. *n*, *A*, *Q* and *m* correspond to the stress exponent, pre-exponential factor activation energy and grain size exponent, respectively (*calculated with X_{H2O}=0.05 wt%). DisGBS: dislocation-accommodated grain boundary sliding. See supplementary material for references.

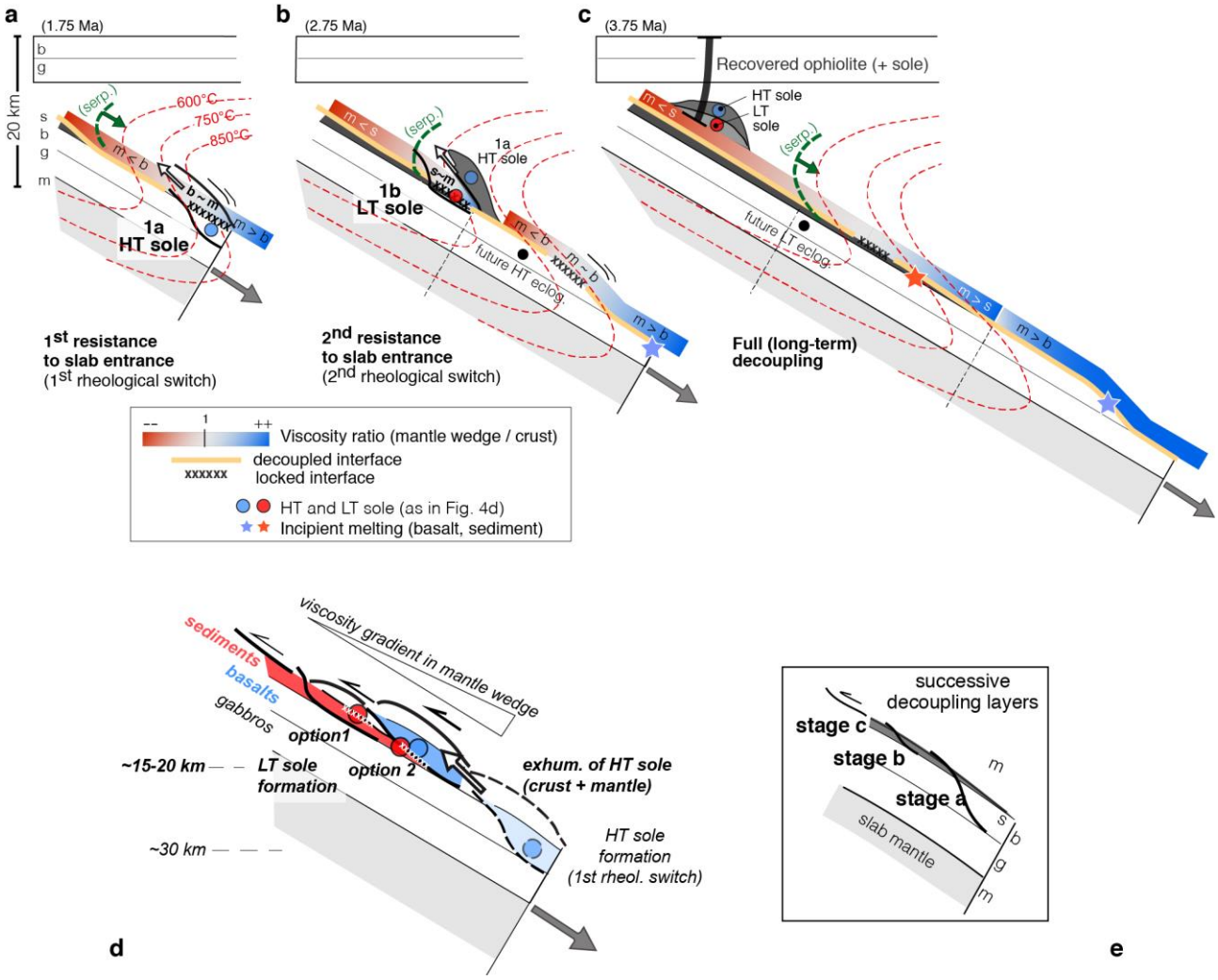


Figure 5

Model evolution for slab penetration and metamorphic sole formation during subduction infancy (2D sketches and abbreviations as in Fig. 4c; the dashed green line marks the downdip limit of the stability of serpentine, "serp."; the white arrow indicates exhumation): (a) strong interplate mechanical coupling due to the first rheological switch (i.e., when mantle wedge viscosity ~ slab basalt viscosity). Resistance of the mantle wedge to slab penetration triggers the peeling of the slab and HT sole formation. Isotherms and depths are from thermo-kinematic modelling (see supplementary material). Stars indicate incipient melting of basalts and sediments (and plagiogranite formation; Rioux et al., 2013); (b) second rheological switch and LT sole formation. HT metabasalts metamorphosed deeper down in the locked zone are not returned as HT soles (see section 5.2.1). Some HT eclogites may get embedded in a softer mantle wedge and exhumed early in the subduction process; (c) the plate interface progressively 'unzips' by the downward extension of serpentinization until full decoupling. P-T-rheological conditions are such that LT eclogites form along the subduction zone but are only rarely exhumed (see section 5.2.1); (d) close-up view on the tectonic configuration along the plate interface during LT sole accretion, when partial exhumation of the HT sole (shown by the white arrow) juxtaposes it onto the LT sole. Accretion of the LT sole may correspond to the mechanical coupling of the sediments with the mantle above (second rheological switch; option 1) or to the mechanical coupling of the sediments with a progressively weakened mafic HT sole (option 2). See text for details. (e) progressive strain localization results in more superficial decoupling over time within the slab, so that accretion becomes restricted after a few My to shallow near-trench infill;

APPENDIX. SUPPLEMENTARY MATERIAL

A. Effective viscosities of plate interface material constrained by rock mechanics

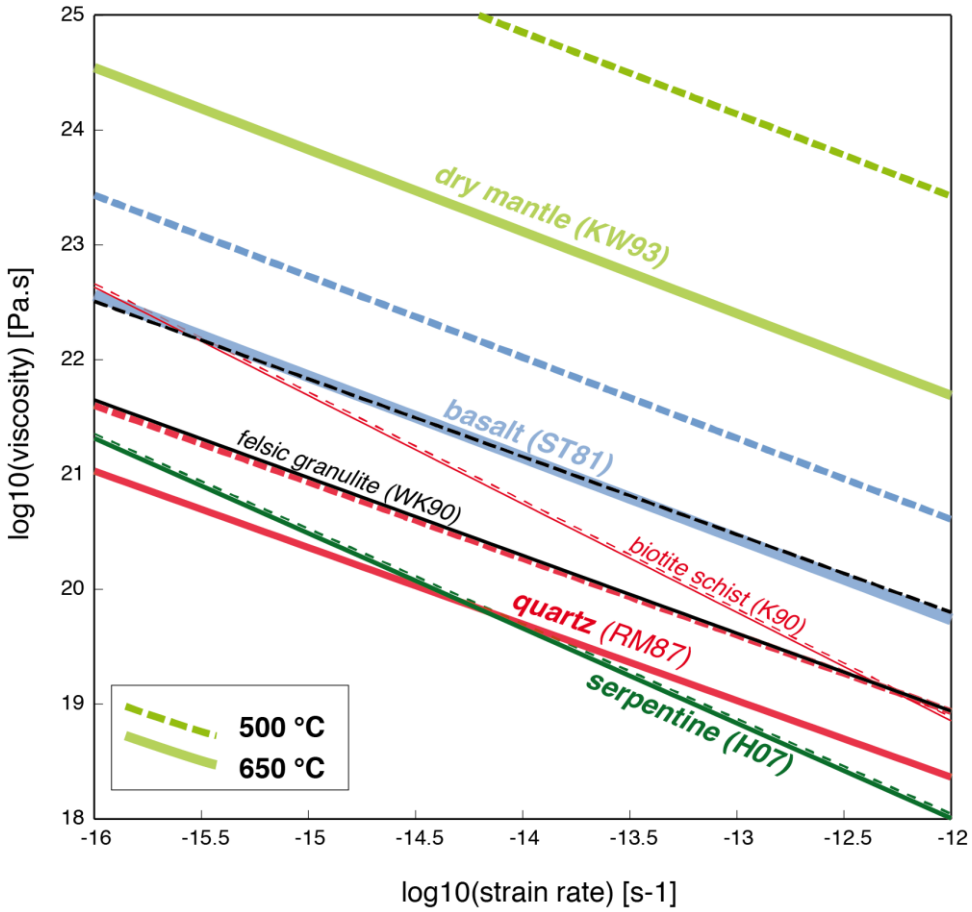


Figure S1. Influence of strain rate on the effective viscosities of selected lithologies at two different temperatures (i.e., 500 and 650°C; same colors as in figure 4a, except for felsic granulite). Note that the respective positions of the dry mantle, basalt, quartz and serpentine remain unchanged for strain rates > ~10^{14} s^{-1}. Note the stronger dependence on strain rate of serpentine and biotite schist, which are almost independent of temperature (as seen in Fig. 4a). Abbreviations: H07: Hilairet et al., 2007; Karato and Wu, 1993; K90: Kronenberg et al., 1990; RM87: Ranalli and Murphy, 1987; ST81: Shelton and Tullis, 1981; WK90: Wilks and Carter, 1990.

B. Thermo-kinematic modelling

Thermo-kinematic modelling (after Duprat-Oualid et al., 2013) was performed here in order to place first order constraints on the thermal regime of our tentative reconstruction of slab penetration into the mantle and metamorphic sole formation (Fig. 5). The advantage of such a 2D thermo-kinematic model, as described in detail in Duprat-Oualid et al. (Fig. S2; 2013), is that it includes a minimum of parameters (i.e., initial thermal ages of the oceanic lithosphere, convergence velocities and slab dips; Fig. S3), in contrast with thermo-mechanical modelling, which is beyond the scope of this study. It also provides a first grip on the depth and duration of the rheological switches outlined in our study (see Fig. S4 below).

1. Model design and numerical code description

The morphology of the model is shown in figure S2a. Incoming lower plate material, with a characteristic initial age for the oceanic lithosphere (T_{age}), is continuously buried at a constant convergence velocity (V) along a subduction plane with prescribed dip angle (θ), to simulate the subduction of an initially flat oceanic lithosphere down to the mantle. The model box is 85 km high, and the width of the model is adjusted depending on θ to ensure a constant grid resolution of 1 km in all models.

The initial temperature is computed following a half space oceanic geotherm equation (e.g., Turcotte and Schubert, 2002), expressing the temperature T as a function of depth (z). Such a thermal profile depends on the thermal properties of the rocks (i.e., k, ρ and Cp), on the thermal age T_{age} of the oceanic lithosphere and on the difference between the temperature of the mantle T_m and the surface T_s, fixed at 1350°C and 0°C, respectively. Thermal properties used both for this initial thermal profile and during the simulations are: k = 2 W.m^{-1}.K^{-1}, ρ = 3000 kg.m^{-3} and Cp = 1000 J.kg^{-1}.K^{-1}.

At each time step, the code solves the following heat thermal equation:

$$\rho \cdot C_p \cdot \frac{\partial T}{\partial t} = \frac{\partial}{\partial x}\left(k\frac{\partial T}{\partial x}\right) + \frac{\partial}{\partial z}\left(k\frac{\partial T}{\partial z}\right) + Q \ , \qquad \text{(Eq. 1)}$$

where ρ, *Cp*, and *k* are the density, the heat capacity and the thermal conductivity, respectively. *Q*, which corresponds to the heat production part (due, for instance, to radiogenic heat production or shear heating), is set to 0. This point is however discussed below and in the discussion section.

This equation (Eq. 1) is solved by using the implicit finite difference method on the Eulerian grid (e.g., Gerya, 2010). Temperature at the top of the model is fixed at 0°C, while the left and right sides of the model are subject to insulating boundary conditions (i.e., $\frac{\partial T}{\partial x} = 0$). The boundary condition at the bottom of the model is that of a constant flux (i.e., $\frac{\partial^2 T}{\partial z^2} = 0$). The temperature *T* computed on the nodes is then interpolated on markers and advected through the model by following the imposed velocity field (see Gerya, 2010 and Duprat-Oualid et al., 2013).

2. Parametric study

The influence of the convergence velocity *V*, subduction dip angle θ and initial age of the oceanic lithosphere T_{age} (controlling the initial thermal profile, Eq. 2) has been tested through a parametric study. For the sake of clarity, we focus the following description on the range of temperatures associated with HT sole formation (for which refined constraints on their P-T conditions of formation also exist; Fig. 3b).

Results show that the kinematic parameters (*V*, θ) control the time at which the tip of the slab reaches a given temperature (Fig. S2c), while the initial thermal age of the oceanic lithosphere controls the depth where this occurs (Fig. S2b). Considering a velocity of 3 cm.yr^{-1} and a dip of 30 $^{\circ}$ for the subducting slab (*V*.sin(θ) is 1.5 cm.yr^{-1}), a very low initial T_{age} is required to reach 700°C in less than ~2 My (Fig. S2b). This is why our reference experiment uses a T_{age} of 3 Ma. In such a

949 configuration, our models predict that the temperature of ~750°C will be reached at around 20 km
950 depths (Fig. S2d).
951
952 **3. Results from modelling**
953 The initial thermal age, convergence velocity and slab dip are set to 3 Ma, 3 cm.yr^{-1} and 30° in
954 the reference model, so that the tip of the oceanic crust located on top of the slab reaches 750°C and
955 20 km depth after ~1.5 My (and 1000°C at ~25 km depth after 1.75 My; Fig. S2d). This
956 configuration is the one adopted in Figure 5.
957 Thermo-kinematic models constrain the evolution of temperature through time along the plate
958 interface for given depths, shown here at 10-20-30-40 km for the reference experiment (Fig. S3a).
959 T-time trajectories of evenly spaced incoming rocks (i.e., at the slab tip and then every 30 km away,
960 for points A, B, C and D; Fig. S1d) are shown on figure S3b.
961 The evolution of temperature through time along the plate interface and T-time trajectories (Fig.
962 S3) show that a rock starting to subduct 1 My after subduction initiation (point B; Fig. S4) will be
963 in the temperature range of formation of the HT sole and mafic/ultramafic rheological switch
964 (~750-850°C) between 2.8 and 3.2 My at 27-32.5 km depth. The depth and duration over which
965 incoming rocks remain in this temperature interval, for a range of realistic upper plate thermal ages
966 and slab dips (Fig. S4), is 25±7 km (across a few km on either side of the thrust) for no more than
967 0.3-0.4 My.
968
969 **4. Influence of shear heating.**
970
971 Shear heating *(Hs)* corresponds to the transformation of mechanical energy into heat during
972 deformation and depends on the strain rate and on the viscosity. For a shear zone with thickness h,
973 exhibiting a homogeneously distributed shear velocity V and an effective mean viscosity η, Hs can
974 be expressed as (e.g., Duprat-Oualid et al., 2015):
975 $$Hs = \eta \frac{V^2}{h^2},$$

In our simulations, we can thus compute this heat production for a given viscosity and a given strain rate as presented in figure S5. Results show that *Hs* strongly affects the thermal evolution around shear zones, especially for high viscosity values. The temperature conditions for the formation of the metamorphic sole are in this case located at shallower depth than in experiments which do not include shear heating. This results are obtained for constant viscosity and do not account for the T-dependency of viscosity: in nature, however, almost all materials (see Fig. 4b) present a decrease in viscosity with increasing temperature. These simulations therefore provide an estimate of the maximum influence of shear heating, reality being probably between situations shown in figures S2d and S5.

The important result is that, even if shear heating highly modifies the thermal field evolution around the shear zone, it does not alter the pattern of the isotherms. Figure S5 indeed shows that whatever the viscosity of the shear zone (and therefore the amount of heat produced by shear heating), the global "S-shape" of the isotherms, and therefore the existence of rheological switches, is always reproduced. Consequently, although shear heating can impact the depth of metamorphic sole formation, it does not affect the processes related to plate interface rheological switches that we propose in this study.

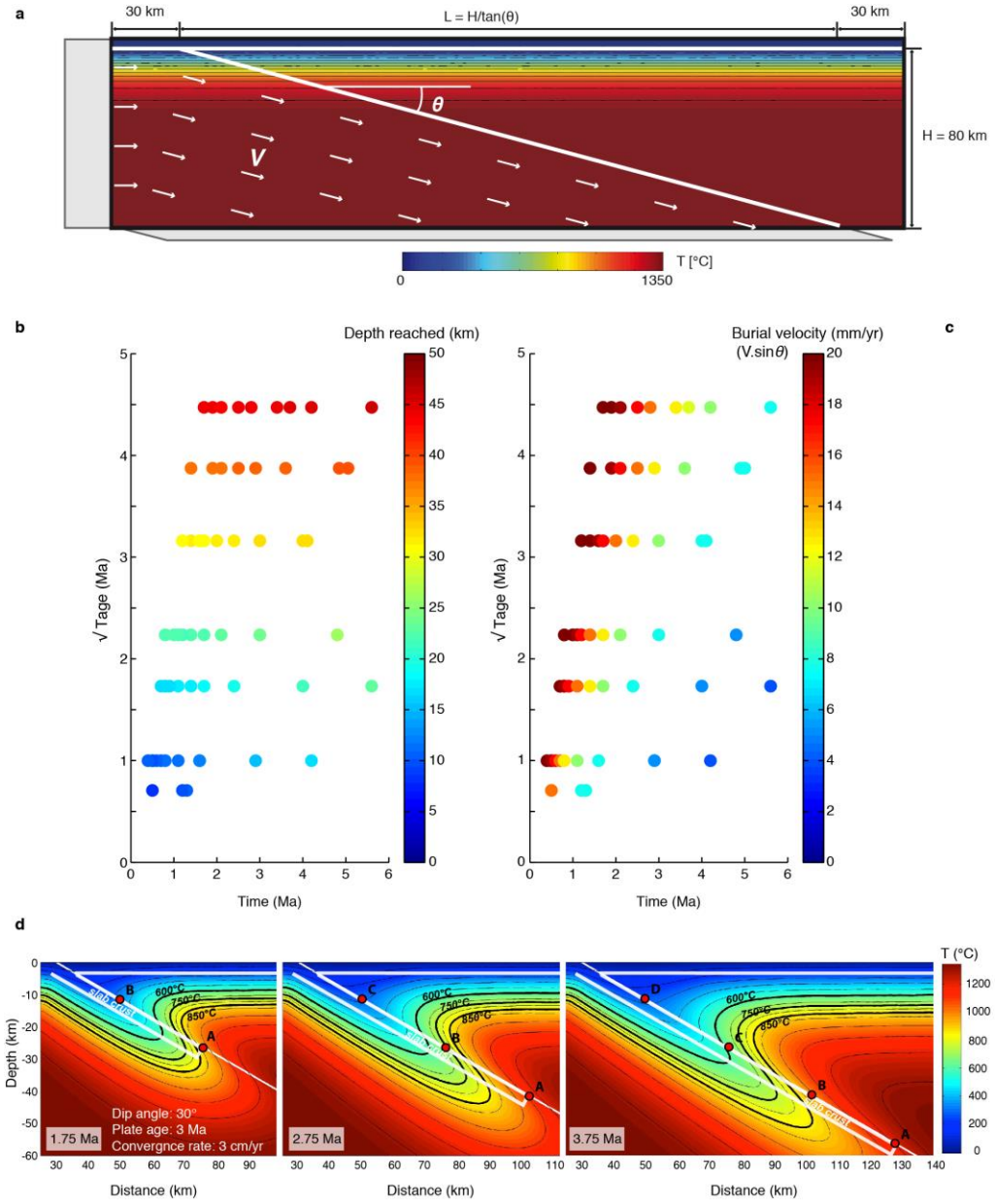


Figure S2. Thermo kinematic modelling of the temperature field associated with slab penetration into the mantle during subduction infancy; (a) Set-up of the numerical model. The initial temperature field is flat and depends on the thermal age of the oceanic lithosphere (T_{age}). V corresponds to the convergence velocity; (b) and (c): Variations, as a function of time and initial oceanic T_{age}, of the depth (left panel) and burial velocity ($V.\sin\theta$; right panel) required for the tip of the slab to reach the temperature of 700°C. Depths of metamorphic sole formation are chiefly controlled by the initial T_{age} of the oceanic lithosphere (left panel), while kinematic parameters control the time at which this happens (right panel); (d) Thermal structure of the reference model after 1.75, 2.75 and 3.75 Myrs, which was used in figure 5.

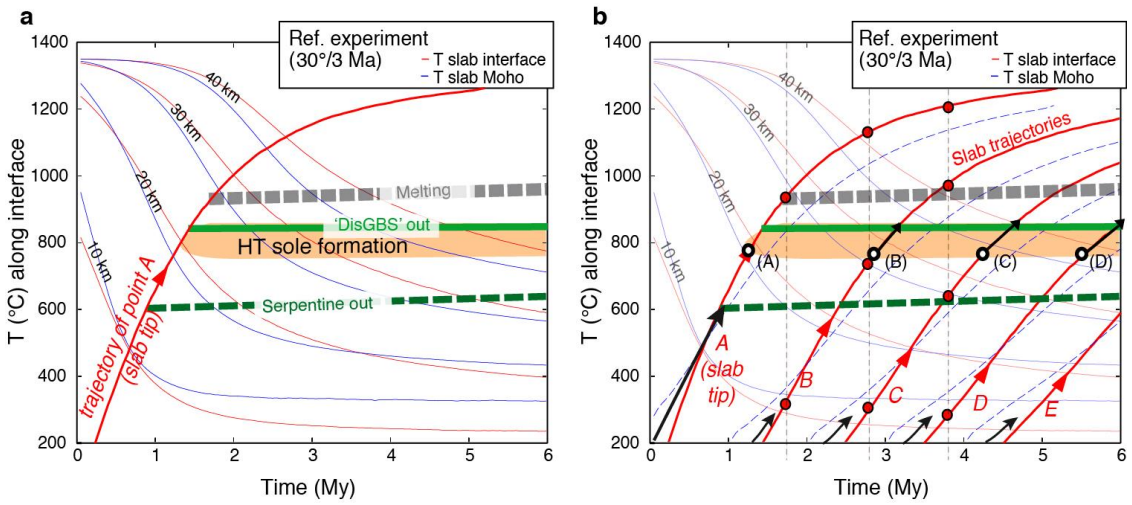


Figure S3. Thermal modelling of slab penetration during subduction infancy. (a) Evolution of slab temperatures along crust-mantle boundaries at depths of 10-20-30-40 km (thin curves). Red line: T-time trajectory of the surface temperature of point A (tip of the slab). Orange overlay: T range of HT sole formation. Incipient melting of basaltic crust is given for an average value between wet and dry MORB (Kessel et al., 2005). See text for deformation mechanisms (disGBS: dislocation-accomodated grain boundary sliding; Linckens et al., 2011a; Hirth and Kohlstedt, 2015); (b) Thick red lines give T-time trajectories for evenly spaced points along the top of the slab (A: slab tip; points A to E are spaced every 30 km; see Fig. S2d). Temperatures along the slab Moho are shown with dashed blue lines. Open black circles indicate when a given point enters the conditions of metamorphic sole formation (black arrows outline approximate duration under these conditions).

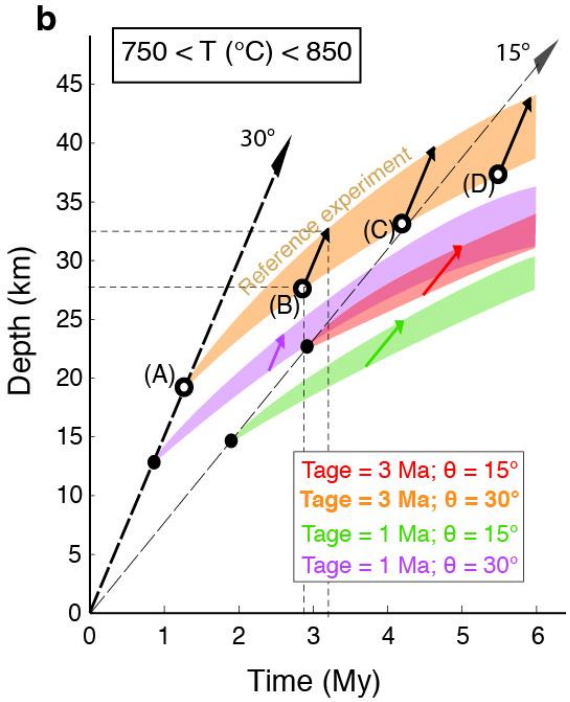


Figure S4. Duration and depth over which incoming rocks remain between 750 and 850°C, during the first rheological switch and HT sole formation (Fig. 4d), depending on upper plate thermal age and slab dip. For the reference experiment, incoming crustal rocks may cross the temperature range of HT sole formation (~750-850°C) at depths of ~25-35 km: accretion of individual slices may last on the order of 0.3-0.4 My, while ~1-3 My would be required to fully accrete the first incoming 100 km of crust on the top of the slab (A to C or D; see text, section 5.2.i for further discussion).

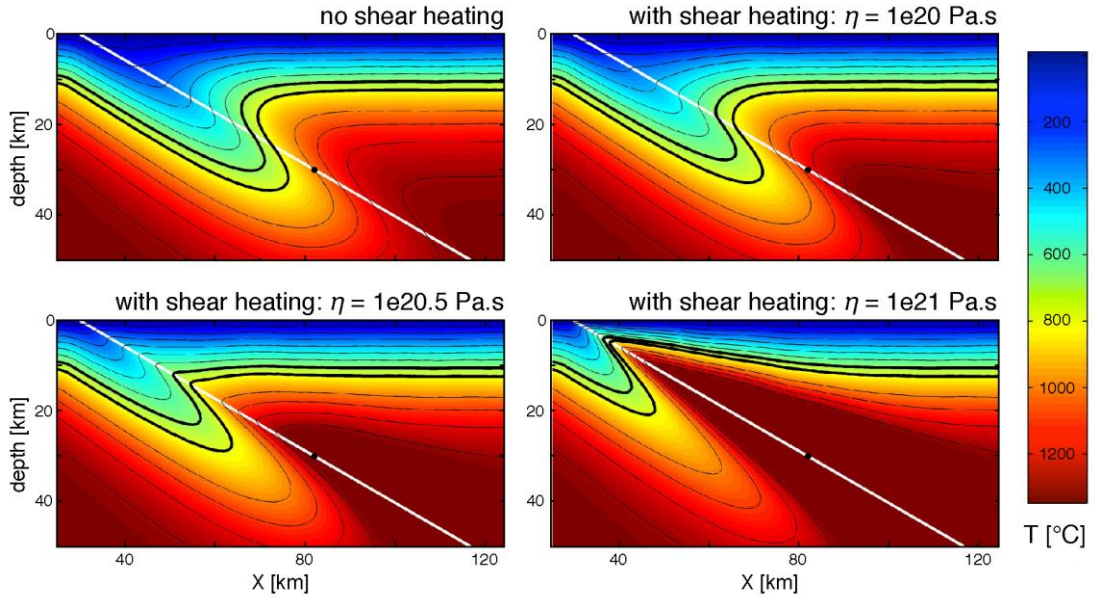


Figure S5. Influence of shear heating on the thermal evolution of the subduction zones. Plots are provided here after 2 My (see details in the supplementary material section 4 above). The top-left panel corresponds to the thermal field obtained for the reference model, with no shear heating. In the 3 others panels, heat production by shear heating is implemented assuming a shear zone thickness of 1 km and a constant viscosity (10^{20}, $10^{20.5}$ and 10^{21} Pa.s, respectively). As the viscosity of rocks is strongly temperature dependent (Fig. 4b), these simulations are not fully consistent but nevertheless useful since the viscosity values considered here lie in the range inferred from natural data (10^{20} Pa.s: Tasaka et al., 2013; 10^{21} Pa.s: Linckens et al., 2011). Black curves correspond to the 700 and 800°C isotherms. The black dot is located at a depth of 30 km for reference.

C. Additional references for the Supplementary material and for Tables 1 and 2

1. Additional references for this Supplementary Material

Duprat-Oualid, S., Yamato, P. & Pitra, P. 2013. Major role of shear heating in intracontinental inverted metamorphism: Inference from a thermo-kinematic parametric study. Tectonophysics 608, 812-831.

Duprat-Oualid, S., Yamato, P., & Schmalholz S.M., 2015. A dimensional analysis to quantify the thermal budget around lithospheric-scale shear zones, Terra Nova, 27, 163-168.

Gerya, T,V., 2010. Introduction to Numerical Geodynamic Modelling, Cambridge Univ. Press.

Turcotte, D.L., Schubert, G., 2002. Geodynamics, 2nd edition. Wiley.

2. References for Table 1

Al-Ryami, K., Robertson, A., Dixon, J. & Xenophontos, C. 2002. Origin and emplacement of the Late Cretaceous Baer–Bassit ophiolite and its metamorphic sole in NW Syria. Lithos. 65, 225-260.

Bucher, M. 1980. Mineral equilibria in metagabbros: Evidence for polymetamorphic evolution of the Asimah windows, Northern Oman Mountains, United Arab Emirates, in Ophiolite Genesis and Evolution of Oceanic Lithosphere. Peters, T., Nicolas, A. & Coleman, R. G. Eds., Kluwer (Dordrecht) 543-571.

Çelik, O. F. & Delaloye, M. F. 2006. Characteristics of ophiolite-related metamorphic rocks in the Beysehir ophiolitic mélange (Central Taurides, Turkey), deduced from whole rock and mineral chemistry. J. Asian Earth Sci. 26, 461-476.

Clague, D., Rubin, J. & Brackett, R. 1981. The age and origin of the garnet amphibole underlying the Thetford-Mines ophiolite. Can. J. Earth Sci. 18, 469-486.

Cluzel, D., Jourdan, F., Meffre, S., Maurizot, P. & Lesimple, S. 2012. The metamorphic sole of New Caledonia ophiolite: 40Ar/39Ar, U-Pb, and geochemical evidence for subduction inception at a spreading ridge. Tectonics. 31, TC3016.

Cowan, R. J., Searle, M. P. & Waters, D. J. 2014. Structure of the metamorphic sole to the Oman Ophiolite, Sumeini Window and Wadi Tayyin: implications for ophiolite obduction processes, Geol. Soc., London Sp. Pub. 392, 155-175.

de Capitani, C. & Brown, T.H. 1987. The computation of chemical equilibrium in complex systems containing non-ideal solutions. Geoch. Cosmochim. Acta 51, 2639–2652.

Dilek, Y. & Whitney, D. L. 1997. Counterclokwise P-T-t trajectory from the metamorphic sole of a Neo-Tethyan ophiolite (Turkey). Tectonophysics. 280, 295-310.

El-Naby, H. A., Frisch, W. & Hegner, E. 2000. Evolution of the Pan-African Wadi Haimur metamorphic sole, Eastern Desert, Egypt. J. Metamorph. Geol. 18, 639-651.

1103 Encarnacion, J. P., Essene, E. J., Mukasa, S. B. & Hall, C. H. 1995. High-pressure and -temperature
1104 subophiolitic kyanite–garnet amphibolites generated during initiation of mid-tertiary
1105 subduction, Palawan, Philippines. J. Petrol. 36, 1481-1503.
1106 Farahat, E. S. 2011. Geotectonic significance of Neoproterozoic amphibolites from the Central
1107 Eastern Desert of Egypt: A possible dismembered sub-ophiolitic metamorphic sole. Lithos. 125,
1108 781-794.
1109 Gaggero, L., Marroni, M., Pandolfi, L., & Buzzi, L. 2009. Modeling the oceanic lithosphere
1110 obduction: Constraints from the metamorphic sole of Mirdita ophiolites (Northern Albania).
1111 Ofioliti. 34, 17-42.
1112 Gartzos, E., Dietrich, V. J., Migiros, G., Serelis, K., Lymperopoulou, T. 2009. The origin of
1113 amphibolites from metamorphic soles beneath the ultramafic ophiolites in Evia and Lesvos
1114 (Greece) and their geotectonic implication. Lithos. 108, 224-242.
1115 Ghent, E. & Stout, M. 1981. Metamorphism at the base of the Samail Ophiolite, Southeastern Oman
1116 Mountains. J. Geophys Res. 86, 2557-2571.
1117 Gnos, E. & Kurz, D. 1994. Sapphirine-quartz and sapphirine-corundum assemblages in
1118 metamorphic rocks associated with the Semail Ophiolite (United Arab Emirates). Contrib.
1119 Mineral Petrol. 166, 398-410.
1120 Gnos, E. 1998. Peak Metamorphic Conditions of Garnet Amphibolites Beneath the Semail
1121 Ophiolite: Implications for an Inverted Pressure Gradient. Int. Geol. Rev. 40, 281-304.
1122 Green, E., Holland, T. J. B. & Powell, R. 2007. An order-disorder model for omphacitic pyroxenes
1123 in the system jadeite-diopside-hedenbergite-acmite, with applications to eclogitic rocks. Am.
1124 Mineral. 92, 1181–1189.
1125 Guilmette, C. et al. 2012. Discovery of a dismembered metamorphic sole in the Saga ophiolitic
1126 mélange, South Tibet: Assessing an Early Cretaceous disruption of the Neo-Tethyan supra-
1127 subduction zone and consequences on basin closing. Gondwana Res. 22, 398-414.
1128 Hacker, B. R. 1994. Rapid Emplacement of Young Oceanic Lithosphere: Argon Geochronology.
1129 Science 265, 1563-1565.

1130 Hacker, B. R. & Mosenfelder, J. L. 1996. Metamorphism and deformation along the emplacement
1131 thrust of the Samail ophiolite, Oman. Earth Planet. Sc. Lett. 144, 435-451.
1132 Hacker, B. R., Mosenfelder, J. L. & Gnos, E. 1996. Rapid emplacement of the Oman ophiolite:
1133 Thermal and geochronologic constraints. Tectonics. 15, 1230-1247.
1134 Hacker, B. R. & Gnos, E. 1997. The conundrum of samail: explaining the metamorphic history.
1135 Tectonophysics 279, 215-226.
1136 Harris, R. A. 1998. Origin and tectonic evolution of the metamorphic sole beneath the Brooks
1137 Range ophiolite, Alaska. Geol. Soc. Am. Spec. Paper. 324, 293-312.
1138 Hassig, M. et al. 2013. New structural and petrological data on the Amasia ophiolites (NW Sevan–
1139 Akera suture zone, Lesser Caucasus): Insights for a large-scale obduction in Armenia and NE
1140 Turkey. Tectonophysics 588, 135-153.
1141 Hassig, M., Rolland, Y. Sosson, M., Galoyan, G., Müller, C. et al. 2015. European Geosciences
1142 Union (EGU) General Assembly, April 27th-May 2nd, Vienna.
1143 Holland, T. J. B. & Blundy, J. 1994. Non-ideal interactions in calcic amphiboles and their bearing
1144 on amphibole-plagioclase thermometry. Contrib. Mineral Petrol. 116, 433-447.
1145 Holland, T. J. B., Baker, J. & Powell, R. 1998. Mixing properties and activity-composition
1146 relationships of chlorites in the system MgO-FeO-Al2O3-SiO2-H2O. Eur. J. Mineral. 10, 395–
1147 406.
1148 Jamieson, R. A. 1981. Metamorphism during ophiolite emplacement—the petrology of the St
1149 Anthony Complex, J. Petrol. 22, 397-443.
1150 Jamieson, R. A. 1986. P-T paths from high temperature shear zones beneath ophiolites. J. Metam.
1151 Geol 4, 3-22.
1152 Lazaro, C. et al. 2013. First description of a metamorphic sole related to ophiolite obduction in the
1153 northern Caribbean: Geochemistry and petrology of the Güira de Jauco Amphibolite complex
1154 (eastern Cuba) and tectonic implications. Lithos 179, 193-210.
1155 Lus, W. Y., McDougall, I. & Davies, H. L. 2004. Age of the metamorphic sole of the Papuan
1156 Ultramafic Belt ophiolite, Papua New Guinea. Tectonophysics 392, 85-101.

1157 Malo, M. Ruffet, G., Pincivy, A. & Tremblay, A. 2008. A 40Ar/39Ar study of oceanic and
1158 continental deformation processes during an oblique collision: Taconian orogeny in the Quebec
1159 reentrant of the Canadian Appalachians. Tectonics 27, TC4001.
1160 McCaig, A. M. 1983. P−T conditions during emplacement of the Bay of Islands ophiolite complex.
1161 Earth Planet. Sci. Lett. 63, 459-473.
1162 Meffre, S. et al. 2012. Basalts erupted along the Tongan fore arc during subduction initiation:
1163 Evidence from geochronology of dredged rocks from the Tonga fore arc and trench. Geochem.
1164 Geophy. Geosyst. 13, Q12003.
1165 Newton, R. C., Charlu, T. V. & Kleppa, O. J. 1980. Thermochemistry of the high structural state
1166 plagioclases, Geochim. Cosmochim. Acta 44, 933-941.
1167 O'Beirne-Ryan, A. M., Jamieson, R. A. & Gagnon, Y. D. 1990. Petrology of garnet-clinopyroxene
1168 amphibolites from Mont Albert, Gaspé, Quebec. Can. J. Earth Sci. 27, 72-86.
1169 Okay, A. I., Harris, N. B. W. & Kelley, S. P. 1998. Exhumation of blueschists along a Tethyan suture
1170 in northwest Turkey. Tectonophysics. 285, 275-299.
1171 Önen, A. P. & Hall, R. 1993. Ophiolites and related metamorphic rocks from the Kütahya region,
1172 north-west Turkey. Geo. J. 28, 399-412.
1173 Önen, A. P. 2003. Neotethyan ophiolitic rocks of the anatolides of NW Turkey and comparison with
1174 Tauride ophiolites. J. Geol. Soc. 160, 947-962.
1175 Pamic, J., Tomljenovic, B. & Balen, D. 2002. Geodynamic and petrogenetic evolution of Alpine
1176 ophiolites from the central and NW Dinarides: an overview. Lithos. 65, 17-42.
1177 Parkinson, C. 1998. Emplacement of the East Sulawesi Ophiolite: evidence from subophiolite
1178 metamorphic rocks. J. As. Earth Sci. 16, 13-28.
1179 Parlak, O. & Delaloye, M. F. 1999. Precise 40Ar/39Ar from the metamorphic sole of the Mersin
1180 ophiolite (southern Turkey). Tectonophysics. 301, 145-158.
1181 Parlak, O., Bozkurt, E. & Delaloye, M. F. 1996. The Obduction direction of the Mersin ophiolite:
1182 structural evidence from subophiolitic metamorphics in the Central Tauride Belt, Southern
1183 Turkey. Int. Geol. Rev. 38, 778-786.

Plunder, A., Agard, P., Chopin, C., Pourteau, A., & Okay, A. I. 2015. Accretion, underplating and exhumation along a subduction interface: From subduction initiation to continental subduction (Tavşanlı zone, W. Turkey). Lithos 226, 233-254.

Powell, R. & Holland, T. J. B. 1999. Relating formulations of the thermodynamics of mineral solid solutions: Activity modeling of pyroxenes, amphiboles, and micas, Am. Mineral. 84, 1-14.

Saccani, E. & Photiades, A. 2004. Mid-ocean ridge and supra-subduction affinities in the Pindos ophiolites (Greece): implications for magma genesis in a forearc setting. Lithos. 73, 229-253.

Savic, G. 1988. Ph-D thesis, University of Houston, Texas.

Searle, M. P. & Malpas, J. 1980. Petrochemistry and origin of sub-ophiolitic metamorphic and related rocks in the Oman Mountains. J. Geol. Soc. 139, 235-248.

Searle, M. P. & Cox, J. 2002. Subduction zone metamorphism during formation and emplacement of the Semail ophiolite in the Oman Mountains. Geol. Mag. 139, 241-255.

Spear, F. S. 1981. An experimental study of hornblende stability and compositional variability in amphibolite. Am. J. Sci. 281, 697-734.

Trzcienski, W. E. 1988. Retrograde eclogite from Mont Albert, Gaspé, Quebec. Can. J. Earth Sci. 25, 30-37.

Warren, C. J., Parish, R. R., Searle, M. P. & Waters, D. J. 2003. Dating the subduction of the Arabian continental margin beneath the Semail ophiolite, Oman. Geology. 31, 889-892.

1205

1206 **3. References for Table 2**

1207

1208 Bussod, G.Y., Katsura, T., Rubie, D.C. 1993. The large volume multi-anvil press as a high P-T
1209 deformation apparatus. Pure Applied Geophys., 141, 579-599.

1210 Chopra, P.N., Paterson,M.S., 1981. The experimental deformation of dunite. Tectonophysics 78,
1211 453–473.

1212 Chopra, P.N., Paterson, M.S., 1984. The role of water in the deformation of dunite. J. Geophys. Res.
1213 89, 7861–7876.

1214 Evans, B. and Kohlstedt, D. L. 1995. Rheology of Rocks. In: Rock Physics & Phase Relations: A
1215 Handbook of Physical Constants (ed T. J. Ahrens), American Geophysical Union, Washington,
1216 D. C., 148-165.

1217 Faul, U. H., Jackson, I. 2007. Diffusion creep of dry, melt-free olivine, J. Geophys. Res., 112,
1218 B04204, doi:10.1029/2006JB004586.

1219 Hacker, B.R. and Christie, J.M. 1990. Brittle/ductile and plastic/cataclastic transitions in
1220 experimentally deformed and metamorphosed amphibolite. Geophysical Monograph 56, 127 -
1221 147

1222 Hilairet, N., Reynard, B., Wang, Y., Daniel, I., Merkel, S., Nishiyama, N., Petitgirard, S. 2007.
1223 High-pressure creep of serpentine, interseismic deformation and initiation of subduction.
1224 Science. 318, 1910-1913.

1225 Hirth, G., Kohlstedt, D.L., 1996. Water in the oceanic upper mantle—implications for rheology,
1226 melt extraction and the evolution of the lithosphere. Earth Planet. Sci. Letters 144, 93–108.

1227 Hirth, G., Kohlstedt, D.L., 2003. Rheology of the upper mantle and the mantle wedge: a view from
1228 the experimentalists. In: Inside the Sub-duction Factory (Ed. Eiler, J.), Geophys. Monogr. 138,
1229 American Geophysical Union, Washington, D.C., 83–105.

1230 Karato, S.-I., Paterson, M.S., Fitzgerald, J.D., 1986. Rheology of synthetic olivine ag-gregates;
1231 influence of grain size and water. J. Geophys. Res.91 (8), 8151–8176.

1232 Karato, S., Wu, P. 1993. Rheology of the upper mantle: a synthesis. Science 260, 771-778.

1233 Karato, S., Rubie, D.C., 1997. Toward experimental study of plastic deformation under deep mantle

conditions: a new multianvil sample assembly for deformation experiments under high pressures and temperatures. J. Geophys. Res. 102, 20111–20122.

Karato, S., Jung, H., 2003. Effects of pressure on high-temperature dislocation creep in olivine. Phil. Mag. 83.

Kawazoe, T., Karato, S., Otsuka, K., Jing, Z.,Mookherjee, M., 2009. Shear deformation of dry polycrystalline olivine under deep upper mantle conditions using a rotational Drickamer apparatus (RDA). Phys. Earth Planet. Int. 174, 128–137.

Kirby, S. H., Kronenberg, A. K. 1987. Rheology of the lithosphere: Selected topics, Rev. Geophys. 25, 1219–1244.

Kronenberg, A. K., Kirby, S. H. & Pinkston, J. C. 1990. Basal slip and mechanical anisotropy of biotite. J. Geophys. Res. 95, 19257-19278.

Li, L., Weidner, D., Ratteron, P., Chen, J., Vaughan, M., Mei, S., Durham, B. 2006. Deformation of olivine at mantle pressure using the D-DIA. Eur. J. Min. 18, 7–19.

Mackwell, S.J., Zimmerman, M.E., Kohlstedt, D.l., 1998. High-temperature deformation of dry diabase with application to tectonics on Venus. J. Geophys. Res. 103, 975–984.

McDonnell, R.D., Peach, C.J., Spiers, C.J. 1999. Flow behavior of fine-grained synthetic dunite in the presence of 0.5 wt% H2O. J. Geophys. Res. 104, 17823–17845.

Mei, S., Kohlstedt, D.L., 2000. Influence of water on plastic deformation of olivine aggregates 2. Dislocation creep regime. J. Geophys. Res.105, 21471–21481.

Ranalli, G., Murphy, D.C., 1987. Rheological stratification of the lithosphere, Tectonophysics 132, 281–295.

Shea, W. T. & Kronenberg, A. K. 1992. Rheology and deformation mechanisms of an isotropic Mica Schist, J. Geophys. Res. 97, 15201-15237.

Shelton, G. & Tullis, J. A. 1981. Experimental flow laws for crustal rocks, Trans. Am. Geophys. Un. 62, 396.

van Hunen, J., van den Berg, A.P. 2008. Plate tectonics on the early Earth: Limitations imposed by strength and buoyancy of subducted lithosphere. Lithos, 103, 217-235.

Wilks, K.R., Carter, N.L., 1990. Rheology of some continental lower crustal rocks. Tectonophysics 182, 57–77.

1266